

Parametric study of two-dimensional potential structures induced by radio-frequency sheaths coupled with transverse currents in front of the Ion Cyclotron Resonance Heating antenna

E. Faudot, S. Heuraux, and L. Colas

Citation: *Physics of Plasmas* **13**, 042512 (2006); doi: 10.1063/1.2186530

View online: <http://dx.doi.org/10.1063/1.2186530>

View Table of Contents: <http://scitation.aip.org/content/aip/journal/pop/13/4?ver=pdfcov>

Published by the *AIP Publishing*

Articles you may be interested in

[Radio-frequency sheaths physics: Experimental characterization on Tore Supra and related self-consistent modeling](#)

Phys. Plasmas **21**, 061509 (2014); 10.1063/1.4884778

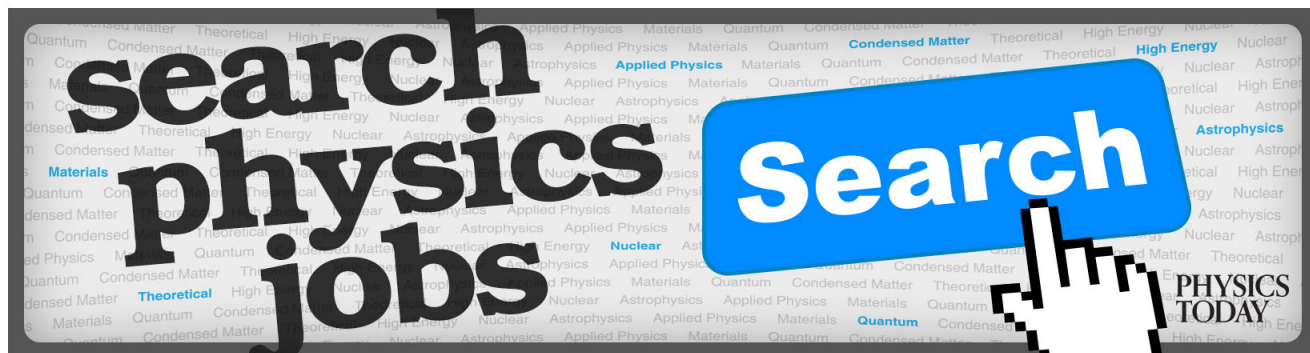
[Broadening of rectified potential structures induced by rf currents in a magnetized plasma: Application to ITER scrape-off-layer](#)

Phys. Plasmas **17**, 042503 (2010); 10.1063/1.3357334

[Compact antenna for two-dimensional beam scan in the JT-60U electron cyclotron heating/current drive system](#)
Rev. Sci. Instrum. **76**, 113504 (2005); 10.1063/1.2130967

[2D modeling of DC potential structures induced by RF sheaths with transverse currents in front of ICRF antenna](#)
AIP Conf. Proc. **787**, 214 (2005); 10.1063/1.2098227

[All-orders spectral calculation of radio-frequency heating in two-dimensional toroidal plasmas](#)
Phys. Plasmas **8**, 1573 (2001); 10.1063/1.1359516



Parametric study of two-dimensional potential structures induced by radio-frequency sheaths coupled with transverse currents in front of the Ion Cyclotron Resonance Heating antenna

E. Faudot and S. Heuraux

LPMIA, UMR CNRS 7040, Université Henri Poincaré, Nancy 1, BP 239,
54506 Vandoeuvre Cedex, France

L. Colas

Association Euratom-CEA pour la fusion Contrôlée, CEA Cadarache,
Saint-Paul-lez-Durance Cedex, France

(Received 16 June 2005; accepted 22 February 2006; published online 25 April 2006)

For the first time, a two-dimensional (2D) fluid model and an analytical expression for the rectified potential with respect to the transverse polarization current are established and verified by a 2D PIC (particle in cell) code over the validity domain of our model. Then the model is extended to the overall ion cyclotron frequency range used in different heating and current drive scenarios. First, the models demonstrate that these transverse polarization currents add some inertia in the temporal dynamic. Due to the nonlinear behavior of the I - V sheath characteristic, the time average amplitude (dc potential) of the rectified potential structure is increased compared to the time average rf potential. Second, they induce only a slight widening of the potential structure. Such modifications are quantified using a “test map” initially characterized by a Gaussian shape. The map is assumed to remain Gaussian near its summit. The time behavior of the peak can be estimated analytically in the presence of polarization current as a function of its width r_0 and amplitude ϕ_0 (normalized to local temperature and to a characteristic length for transverse transport). A potential peaking criterion has been built to determine the peaking zone of the dc potential structure induced by the rf field. Computations made for typical parameters of the edge plasma in front of the antenna of the Tokamak Tore Supra show that the dc rectified potential is up to 50% higher than the previous computations neglecting polarization current effects. The weak diffused and high dc potential structures computed can explain the hot spot formation induced by convective cells associated to high energetic ion fluxes on the corners of the Ion Cyclotron Resonance Heating antenna. © 2006 American Institute of Physics. [DOI: 10.1063/1.2186530]

I. INTRODUCTION

Most of laboratory and industrial plasmas are confined in finite metallic devices. The interaction between the confined neutral plasma and the material walls is driven by a thin space charge layer, i.e., the sheath.

At equilibrium, the sheath maintains the neutrality of the plasma everywhere around the vessel, so that a free-current system is built. Due to different mobility between electrons and ions, a potential drop appears between the vessel and the core plasma in the sheath region. This potential drop is the floating potential for an unperturbed plasma.

Here we consider the case of magnetized plasma with anisotropic mobility driven by a rf polarization. The sheaths in which the potential is created oscillate by rectifying the rf potential.^{1,2} The whole magnetic line potential follows the potential imposed by rf sheaths. The suppression of the negative component of the rf potential along the field line by rf sheaths can give high dc potential structures^{3,4} supposing the wall potential is 0 V. These dc potential distributions can first increase the power deposition on the wall and induce convective fluxes to produce hot spots on and around the antenna structure. This work was first motivated by the hot spot appearing in the corner of the ICRH antenna in the

Tokamak Tore Supra.⁵ This kind of phenomenon has been observed in other Tokamaks as well and results from high power deposition associated with fast particles on the antenna structure.

To evaluate the power deposition, there is a clear necessity to determine the sheath potential self-consistently, taking into account the significant contributions of the rf potential map. The rf potential results from the integration along the magnetic field lines of the parallel component of the radiated electric field by the antenna. The chosen magnetic field topology corresponds to the description of magnetic field lines existing between both bumpers surrounding the antenna. The potential along a magnetic field line looks constant except in the sheath zone. The radiated electric field in front of the antenna exhibits high spatial variations and generates perpendicular rf potential gradients. These transverse gradients induce rf polarization currents, which consequently change the rectified potential structure.⁶

The rectification of rf potential due to asymmetrical inertia of ions and electrons in sheaths⁷ and parallel dynamic of rf sheaths⁸ has been studied in previous works. For example, the transient dynamics of sheaths in unmagnetized plasma have been examined with fluid models.⁹ Other approaches using fluid models have taken into account trans-

verse currents due to collisions both in the case of Langmuir probes^{10–13} with an approximation of scale lengths for currents¹⁴ and in the case of edge plasmas in Tokamaks.¹⁵ Flux tubes exchanging dc current have been modeled through an electric circuit characterizing the parallel capacitance of sheaths.¹⁶ Other studies, including this work, deal with rf sheaths driven by ICRH and use a fluid model including transverse currents.^{17–19} As these currents, however, come exclusively from the dc component of the rectified potential, the contributions of the rf polarization currents are neglected.

Based on the crude modeling built to describe the hot spots,²⁰ a general model describing the sheaths has been developed including the new term associated with the transverse rf polarization current. This contribution has generally been overlooked in other sheath models. Here we describe its impact on the rf polarization of a flux tube and explain its nonlinear behavior. As a consequence, we are able to extract precisely the dc potential for each flux tube in a plane perpendicular to the magnetic field.

The aim of this work is to evaluate quantitatively and self-consistently the rectified potential dynamics due to rf transverse polarization currents, and then apply it to a real case. In the first section, a simple “flux tube model with transverse polarization currents” is developed. In the ensuing section, the analytical results are compared to numeric computations [2D fluid code and 2D space/3D velocity particle in cell (PIC) code] of the rectified potential. The PIC code is also used to extend the results of our model over the ion cyclotron frequency range used in the heating and current drive scenarios. Our model is finally applied to the case of a Tokamak edge plasma driven by the rf electric field radiated by an ICRH antenna in order to explore the hot spot issue. A potential peaking criterion is defined as a function of characteristic plasma parameters for the case of the ICRH Tore Supra antenna.

II. MODELING AND ANALYTICAL RF RECTIFIED POTENTIAL WITH TRANSVERSE CURRENTS

A. Basic description of rf sheaths

We assume that the plasma behaves as a homogeneous medium along a magnetic field line and that the magnetic field intensity is constant. Modeling of the potential behavior in a plane perpendicular to a magnetic field in front of antennas is achieved by using a flux tube able to exchange current with its neighbor. This flux tube represents the plasma along an open magnetic field line (OMFL) located between the antenna’s bumpers in our particular case. The sheaths appear at the ends of an OMFL, in a small layer near the material surface of the bumpers represented by electrodes in Fig. 1. The presheath physics is ignored because the loss of potential in this collisional space charge is negligible relative to rf potential. In addition, the magnetic field is perpendicular to the wall, canceling the potential effect of the magnetic presheath. If we consider that electrodes at each end of the magnetic line have the same properties and then play a symmetrical role, we obtain the electric model by putting the ground between two symmetric sources of tension (see Fig.

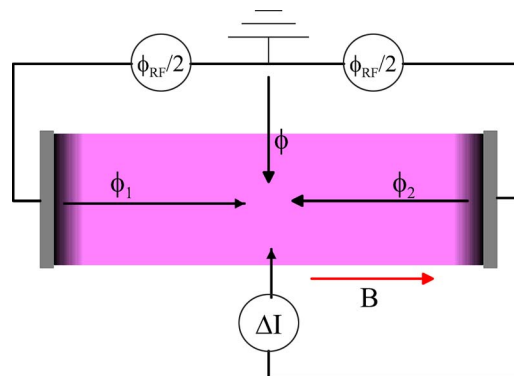


FIG. 1. (Color online) Scheme of one flux tube model with transverse current.

1). This kind of electric circuit used for double probe modeling is widely used in discharge plasmas. This modeling is useful to obtain a simple analytical solution in the case of low frequency compared to ion cyclotron frequency.²¹ It will be shown below (Sec. III C) that the choice of the ground position is crucial. Here, a symmetric circuit was chosen, because it seems to be the most realistic configuration. Nevertheless, a rigorous demonstration has to be done to define the importance of the ground in the case of a rf sheath driven by rf electric fields. The assumption is made that the model is electrostatic and the rf pulsation ω is smaller than the plasma pulsation $< \Omega_{pi}$, so that the parallel inertia of the sheath can be neglected. Moreover, plasma density is supposed to be constant, and electrons follow the Boltzmann law. Doing so, we can apply current conservation [expression (1)] with a double-probe model to which transverse currents have been added,

$$\nabla \cdot (j_p + j_\perp) = 0. \quad (1)$$

Here j_p is the parallel current density and j_\perp is the transverse current density.

The Boltzmann electron density distribution $n_0 \cdot \exp(-eV/T_e)$, with n_0 the plasma density, e the electron charge, V the electrostatic potential, and T_e the electron temperature in eV, associated with $j_{\text{isat}} = e \cdot n_0 \cdot C_s$ with C_s the ion sound velocity, leads to the I - V characteristic for a double probe integrated over one flux tube with a “flute hypothesis,”

$$j_{\text{isat}} - j_{\text{esat}} \exp(-\phi + \phi_{\text{rf}}/2) + j_{\text{isat}} - j_{\text{esat}} \exp(-\phi - \phi_{\text{rf}}/2) + L_p \nabla_\perp \cdot j_\perp = 0. \quad (2)$$

j_{isat} and j_{esat} are, respectively, ion and electron saturation current densities, ϕ is the potential of the plasma compared to the ground, and ϕ_{rf} is the rf potential resulting from the integration of the parallel electric field E_{rf} along an OMFL. For all calculations, ϕ and ϕ_{rf} are normalized to T_e/e , and depend on the time t and the spatial coordinate r in a cylindrical geometry. The \mathbf{P} direction is along B_0 and the \perp direction is perpendicular to B_0 . The I - V characteristic equation (2) is rewritten as follows to simplify further analyses:

$$\frac{j_{\text{esat}}}{2j_{\text{isat}}} \left(\exp \frac{\phi_{\text{rf}}}{2} + \exp -\frac{\phi_{\text{rf}}}{2} \right) = \left(1 + \frac{L_P \nabla_{\perp} \cdot j_{\perp}}{2j_{\text{isat}}} \right) \exp \phi. \quad (3)$$

The logarithm of Eq. (3) gives Eq. (4) expressing the rectified potential ϕ as a function of the driven rf potential ϕ_{rf} and the transverse current j_{\perp} ,

$$\phi = \ln \left(\frac{j_{\text{esat}}}{j_{\text{isat}}} \right) + \ln \left[\cosh \left(\frac{\phi_{\text{rf}}}{2} \right) \right] - \ln \left(1 + \frac{L_P \nabla_{\perp} \cdot j_{\perp}}{2j_{\text{isat}}} \right). \quad (4)$$

The time average rectified potential appearing in Eq. (5) adds interesting information about the behavior of this potential with respect to a generalized perpendicular current j_{\perp} ,

$$\langle \phi \rangle_t = \ln \left(\frac{j_{\text{esat}}}{j_{\text{isat}}} \right) + \frac{1}{T} \int_0^T \ln \left[\cosh \left(\frac{\phi_{\text{rf}}}{2} \right) \right] dt - \frac{1}{T} \int_0^T \ln \left(1 + \frac{L_P \nabla_{\perp} \cdot j_{\perp}}{2j_{\text{isat}}} \right) dt. \quad (5)$$

Then each term of Eq. (5) is evaluated supposing that the transverse current is periodic and that its time average value is equal to 0 [Eq. (6)], irrespective of the frequency and the shape of the signal, T is the period of j_{\perp} , and ϕ_{rf} supposed sinusoidal:

$$\frac{1}{T} \int_0^T j_{\perp} dt = 0, \quad (6)$$

$$\ln \left(\frac{j_{\text{esat}}}{j_{\text{isat}}} \right) = \phi_{\text{fl}}, \quad (7)$$

$$\frac{1}{T} \int_0^T \ln \left[\cosh \left(\frac{\phi_{\text{rf}}}{2} \right) \right] dt = \frac{\phi_{\text{rf}}}{\pi} - \ln 2, \quad (8)$$

$$\frac{1}{T} \int_0^T \ln \left(1 + \frac{L_P \nabla_{\perp} \cdot j_{\perp}}{2j_{\text{isat}}} \right) dt < 0. \quad (9)$$

Expression (7) is the floating potential. Expression (8) shows that the time average value of the rectified potential without transverse current is equal to $\phi_{\text{rf}}/\pi - \ln 2$ for $\phi_{\text{rf}} \gg 1$. Finally, expression (9) demonstrates that the component including a transverse current with a null time average value is always negative with the only assumption of Eq. (6). In that case, this means that the current j_{\perp} always increases the dc rectified potential $\langle \phi \rangle_t$.

The dc rectified potential can even be calculated by supposing that $L_P \nabla_{\perp} \cdot j_{\perp} / 2j_{\text{isat}} = b \cdot \sin(\omega t)$,

$$\begin{aligned} & \frac{1}{\pi} \int_{-\pi/2}^{\pi/2} \ln[1 + b \cdot \sin(\omega t)] d\omega t \\ &= - \sum_{n=1}^{\infty} \frac{b^{2n}}{2n} \frac{(2n-1)!!}{2n!!} \pi \quad \text{for } |b| < 1. \end{aligned} \quad (10)$$

Equation (10) confirms the increase of the dc rectified potential due to sinusoidal transverse current with a time average value equal to 0. The periodic rf transverse current is actually

far from sinusoidal, as shown later on, nevertheless this equation gives a good approximation of the behavior of the time average potential.

B. Fluid model with transverse dynamics

The standard working conditions of an Ion Cyclotron Resonance Heating antenna in continuous wave (CW) mode correspond to a configuration where the ion cyclotron resonance and the wave hybrid resonance are far from the antenna structure due to magnetic field inhomogeneity. As the resonances are remote from the antenna and because the plasma surrounding the antenna has a low temperature around 20 eV, the wave propagation can be described according to cold plasma approximation.²² This assumption will be validated afterwards by comparison between PIC simulations and our rf sheath model. If the resonances become closer to the antenna structure, the finite Larmor radius corrections are required to evaluate the polarization current. However, this situation corresponds to a nonrelevant ITER condition not considered here because the heat load on the antenna structure becomes irrelevant for steady-state scenarios.

The purpose here is to extend the flux tube model to a 2D fluid model. Most of the fluid models on the rf sheath derive from discharge plasmas, mainly in unmagnetized plasmas, to obtain spatiotemporal data and energy distributions in the sheath^{23,24} or to study the response of rf sheaths at different frequencies. In these cases, only parallel dynamics of sheaths is appraised. The model is built to calculate self-consistently the transverse rf polarization currents between flux tubes. This is a notable improvement compared to the latest works that consider transverse dc currents to ultimately calculate the convective flux in the edge plasma of Tokamaks.¹⁹ Thus, we introduce and describe the transport term for transverse current j_{\perp} with respect to space and time. The plasma is supposed to be homogeneous in density. That is why only the motion equation for each species is needed here to calculate the perpendicular current j_{\perp} ,

$$\begin{aligned} nm \left(\frac{\partial \mathbf{v}}{\partial t} + \mathbf{v} \cdot \nabla \mathbf{v} \right) &= -\nabla p + nq(\mathbf{e} + \mathbf{v} \times \mathbf{B}_0) \\ &\quad - \nabla \cdot \pi - F_{ei} - nm\nu_c \mathbf{v}. \end{aligned} \quad (11)$$

In Eq. (11), n is the plasma density, m is the mass for each species, \mathbf{v} is the velocity for each species, p is the pressure, $\mathbf{E} = -\nabla V$ is the rf electronic field, B_0 is the magnetic field, π the viscosity tensor, F_{ei} the force resulting from collisions between ions and electrons, and ν_e the collision frequency between the charged particles with neutrals. The equation can be considerably reduces if we consider isothermal plasma with no viscosity.

By simply solving $\mathbf{E} + \mathbf{v} \times \mathbf{B}_0 = 0$, we obtain the magnetic drift velocity,

$$\mathbf{V}_D = \frac{\mathbf{E} \times \mathbf{B}_0}{B_0^2} = \frac{\mathbf{B}_0 \times \nabla V}{B_0^2}. \quad (12)$$

This is the main component of the perpendicular velocity in equation

$$\mathbf{v}_{i,e} = \mathbf{v}_D + \delta\mathbf{v}_{i,e}. \quad (13)$$

Now, the perpendicular current can be deduced simply by replacing \mathbf{v} by

$$\mathbf{v}_D + \delta\mathbf{v}.$$

The current components are described in Eqs. (14)–(18), where j_{\perp}^{pol} is the polarization current due to the time differential inertia between ions and electrons, j_{\perp}^{conv} is the convective current due to the spatial differential inertia between ions and electrons, j_{\perp}^{fei} is the conduction current due to collisions between ions and electrons, and j_{\perp}^{feiN} is the conduction current due to collisions between ions and electrons with neutrals for which the average velocity is zero,

$$\mathbf{j}_{\perp} = \mathbf{j}_{\perp}^{\text{pol}} + \mathbf{j}_{\perp}^{\text{conv}} + \mathbf{j}_{\perp}^{\text{fei}} + \mathbf{j}_{\perp}^{\text{feiN}}, \quad (14)$$

$$\mathbf{j}_{\perp}^{\text{pol}} = \frac{n_0 \mathbf{B}_0}{B_0^2} \times \left[m_i \left(\frac{\partial \mathbf{v}_D}{\partial t} \right) + m_e \left(\frac{\partial \mathbf{v}_D}{\partial t} \right) \right], \quad (15)$$

$$\mathbf{j}_{\perp}^{\text{conv}} = \frac{n_0 \mathbf{B}_0}{B_0^2} \times [m_i \delta\mathbf{v}_i \cdot \nabla \mathbf{v}_D + m_e \delta\mathbf{v}_e \cdot \nabla \mathbf{v}_D], \quad (16)$$

$$\mathbf{j}_{\perp}^{\text{fei}} = \frac{n_0 \mathbf{B}_0}{B_0^2} \times [m_e \nu_{ei} (\delta\mathbf{v}_i - \delta\mathbf{v}_e)], \quad (17)$$

$$\mathbf{j}_{\perp}^{\text{feiN}} = \frac{n_0 \mathbf{B}_0}{B_0^2} \times [m_i \nu_{iN} \mathbf{v}_D + m_e \nu_{eN} \mathbf{v}_D], \quad (18)$$

ν_{ei} is the ion-electron collision frequency, and ν_{iN} the ion-neutral collision frequency. Such an expression of j_{\perp} was already written^{10,15} to investigate different mechanisms of transverse currents except for polarization current at rf frequencies. Because electron inertia is much weaker than ion inertia, δv_i , δv_e and δv_e can be neglected. On the other hand, the drift velocity v_D is the same for ions and electrons.

$$\mathbf{j}_{\perp} = \frac{n_0 \mathbf{B}_0}{B_0^2} \times \left[m_i \left(\frac{\partial \mathbf{v}_D}{\partial t} + \delta\mathbf{v}_i \cdot \nabla \mathbf{v}_D \right) + m_e \nu_{ei} \delta\mathbf{v}_i + m_i \nu_{iN} \mathbf{v}_D \right]. \quad (19)$$

Here the polarization contribution appears at the first place on the right-hand side (RHS) of Eq. (19).

For \mathbf{B} along the z direction, \mathbf{E} along the x direction, and for velocity gradients only along one direction x (the y velocity is supposed constant), Eqs. (15)–(18) are linearized in the corresponding Fourier space for a simple Cartesian geometry so that $v(\omega, k_x) = v_0 \exp(i\omega t - ik_x x)$. δv_{xi} is the component along x of $\delta\mathbf{v}_i$.

$$\delta\mathbf{v}_i \cdot \mathbf{j}_x(k_x, \omega) = \frac{n_0}{B_0} [m_i i \omega v_D + m_i \delta v_{xi} (-i) k_x v_D + m_e \nu_{ei} \delta v_{xi} - m_i \nu_{iN} v_D]. \quad (20)$$

Each term in Eq. (20) must now be ordered. $m_e \nu_{ei} \delta v_{xi}$ is much lower than $m_i \nu_{iN} v_D$ because $\nu_{ei} \ll \nu_{iN}$ ²⁵ and because δv_{xi} is lower than v_D as supposed in Eq. (13). The second term on the RHS of the same equation corresponds to a convective

current called the inertia current in the Rozhansky model. This term was considered by Carlson¹⁴ in a linear approximation. In this case (as in our case), $\delta v_{xi} k_x v_D$ is greater than $\nu_{iN} v_D$ under the condition that δv_{xi} is greater than ν_{iN} . Finally, the polarization current is much greater than the convective current assuming that ω is much greater than $k_x \delta v_{xi}$. This becomes true for centimetric potential structure [$k_x / (2\pi) \approx 100 \text{ m}^{-1}$] even for high potential value (for $E = 100 \text{ kV/m}$, $v_D \approx 10^5 \text{ m/s}$ for a typical ICRH frequency (in a range of 10–100 MHz)).

In realistic conditions of the Tokamak edge plasma parameters, the polarization currents dominate among all other current components defined in Eq. (14). As a consequence, $\delta\mathbf{v}$ will be substituted by the velocity associated with polarization currents. This polarization speed can be exactly deduced by simply solving the motion equation with the time-dependent speed, the electric force, and the magnetic drift as shown in Eq. (21),

$$m \frac{\partial \mathbf{v}}{\partial t} = q(\mathbf{E} + \mathbf{v} \times \mathbf{B}). \quad (21)$$

In a Fourier space, $v(\omega) = v_0 \exp(i\omega t)$ and $v(\omega)$ can be solved in the simplest 3D Cartesian geometry where $\mathbf{E} = E_x \mathbf{e}_x$ and $\mathbf{B} = B_z \mathbf{e}_z$,

$$\begin{Bmatrix} j_x \\ j_y \\ j_z \end{Bmatrix} = n_0 e^2 E_x \begin{Bmatrix} \frac{i}{m_i} \frac{\omega}{\Omega_{ci}^2 - \omega^2} + \frac{i}{m_e} \frac{\omega}{\Omega_{ce}^2 - \omega^2} \\ -\frac{i}{m_i} \frac{\Omega_{ci}}{\Omega_{ci}^2 - \omega^2} - \frac{i}{m_e} \frac{\Omega_{ci}}{\Omega_{ce}^2 - \omega^2} \\ 0 \end{Bmatrix}. \quad (22)$$

j_x , which is along E_x , is the component for polarization current, whereas j_y is perpendicular to the electric field and is the current associated to the velocity v_D . Then, if the potential structure is along a closed curl, the divergence of j_y is 0 and ultimately implies no current transport. At low frequency, $\omega = \Omega_{ci}$,

$$\delta v_{xi} = \frac{\omega}{\Omega_{ci}} v_D. \quad (23)$$

By replacing δv_{xi} by its expression in Eq. (20), each component of the currents can be displayed,

$$j_x(k_{\perp}, \omega)^{\text{pol}} = n_0 e \frac{i \omega}{\Omega_{ci}} v_D, \quad (24)$$

$$j_x(k_{\perp}, \omega)^{\text{conv}} = -n_0 e \frac{i \omega k_x v_D}{\Omega_{ci}^2} v_D, \quad (25)$$

$$j_x(k_{\perp}, \omega)^{ei} = n_0 e \frac{\nu_{ei} \omega}{\Omega_{ci} \Omega_{ce}} v_D, \quad (26)$$

$$j_x(k_{\perp}, \omega)^{iN} = -n_0 e \frac{\nu_{iN}}{\Omega_{ci}} v_D. \quad (27)$$

This confirms that, for such an expression of δv_{xi} , the conduction current due to collision between ions and neutrals is smaller than convection currents while $\omega k_x v_D / \Omega_{ci}$ is smaller

TABLE I. Typical parameters for an edge plasma of hydrogen in Tokamaks illustrated in Fig. 2.

n_0	10^{18} m^{-3}
T_i	20 eV
T_e	20 eV
ω	6×10^7
Ω_{ci}	rad/s
	2×10^8
ω_{ce}	rad/s
	3×10^{11}
ν_{ei}	10^6 s^{-1}
ν_{iN}	10^4 s^{-1}
k_x	1–1000
v_D	100– 10^6
	m/s
C_s	5×10^4
	m/s

than ν_{iN} , which is the case for the same parameters of Table I. Finally, for typical rf frequencies compared to $\omega k_x v_D / \Omega_{ci}$ still with the parameters of Table I, we verify that polarization currents are much greater than convection currents while the transverse potential gradient length is larger than 1 cm.

Figure 2 depicts the four curves that describe Eqs. (24)–(27), respectively, and demonstrates that our model is valid as long as $k_x v_D / \Omega_{ci}$ remains smaller than 1 for the parameters of Table I, typically with $k_x = 2\pi / r_0 \text{ m}^{-1}$. v_d depends on k_x according to the relation $v_D(k_x) \approx 1001k_x - 901$. This relation enables us to spread the whole typical domain for v_d and k_x at the same time (see Table I).

Now, the transverse current can be expressed by a single dominant term which is the polarization current, with $\delta v = v_D$, that is to say for $\omega = \Omega_{ci}$. The polarization current results from the differential oscillation between ions and electrons in the direction of the potential gradient. This component is periodic with a time average value equal to 0 as previously assumed in Eq. (6),

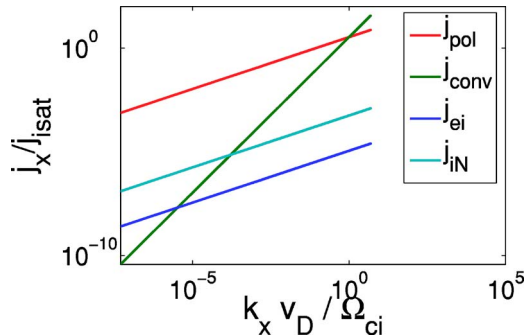


FIG. 2. (Color online) Scaling of transverse currents coming from Eqs.(24)–(27) and normalized to $j_{\text{isat}} = en_0 C_s$ as a function of $k_x v_D / \Omega_{ci}$ with the relation $v_D(k_x) \approx 1001k_x - 901$.

$$\mathbf{j}_\perp = n_0 \mathbf{B}_0 \times \left[m_i \frac{\partial \mathbf{v}_\perp}{\partial t} \right] / B_0^2 = \frac{n_0 m_i}{B_0} \frac{\partial \nabla V}{\partial t}. \quad (28)$$

We evaluate ΔI appearing in Fig. 1 with polarization current for a “flute hypothesis.” This notation introduces the length of the magnetic line.

$$\Delta I = -L_P \nabla_\perp \cdot \mathbf{j}_\perp = -L_P \frac{n_0 m_i}{B_0} \frac{\partial \nabla^2 V}{\partial t}. \quad (29)$$

The expression of the perpendicular current normalized to the ion saturation current is given by Eq. (30),

$$\frac{\Delta I}{2j_{\text{isat}}} = - \frac{L_P \rho_{ci}}{2\Omega_{ci}} \frac{\partial \nabla^2 \phi}{\partial t}, \quad (30)$$

where $\rho_{ci} = C_s / \Omega_{ci}$ is the ion Larmor radius at the sound speed $C_s = \sqrt{Te/m_i}$, $\Omega_{ci} = eB_0/m_i$ is the ion cyclotron frequency, and $\phi = eV/T_e$. If $\phi(t)$ is periodic, the current ΔI described by Eq. (30) has a time average value equal to 0, and then the inequality (9) is valid. We infer the expression of the rectified potential structure from Eq. (3) to which the current term of Eq. (30) is added,

$$\phi(r, t) = \phi_0 + \ln \left[\cosh \left(\frac{\phi_{\text{rf}}(r, t)}{2} \right) \right] - \ln \left(1 + \frac{\Delta I}{2j_{\text{isat}}} \right), \quad (31)$$

$$= \phi_0 + \ln \left[\cosh \left(\frac{\phi_{\text{rf}}(r, t)}{2} \right) \right] - \ln \left(1 - A \frac{\partial \nabla^2 \phi(r, t)}{\partial t} \right) \quad (32)$$

with $A = L_P \rho_{ci} / 2\Omega_{ci}$.

III. PHYSICAL REGIMES OF THE RECTIFIED POTENTIAL DYNAMIC

For the following calculations, we work on a spatial Gaussian potential structure in a cylindrical geometry transversally to the field lines, which oscillates in time with a pulsation ω . r_0 is equal to half the width of the Gaussian potential structure given in the expression (33) and ϕ_0 is its amplitude,

$$\phi_{\text{rf}}(r, t) = \phi_0 \cdot \cos(\omega t) \exp \left(-\frac{r^2}{r_0^2} \right). \quad (33)$$

h'' normalized to half the width of the Gaussian structure, and $\phi_0/2$ half the amplitude of $\phi_{\text{rf}}(r, t)$, with $\tau_\perp = -4A/r_0^2$ (for a Gaussian structure) and $L_{nc}^2 = \omega A$.

The potential term involving polarization currents is

$$\ln \left(1 + \frac{\Delta I}{2j_{\text{isat}}} \right). \quad (34)$$

This term can be linearized for $\Delta I / 2j_{\text{isat}} \ll 1$. Then, one characteristic parameter driving the physical behavior of the rectified potential dynamic is introduced and can be written in two different ways: the characteristic “diffusion length”

$$L_{nc} = \sqrt{\frac{\omega L_P \rho_{ci}}{2\Omega_{ci}}} \quad (35)$$

normalized to half the width of the Gaussian structure r_0 and

$$\omega\tau_{\perp} = -\frac{4\omega L_p \rho_{ci}}{2\Omega_{ci} r_0^2} \quad (36)$$

the normalized “characteristic relaxation time.” The temporal parameter $\omega\tau_{\perp}$ is relevant to study the temporal dynamic and the spatial parameter L_{nc}^2/r_0^2 is useful to investigate the spatial behavior of the Gaussian potential structure.

A. Linear regime

If $\Delta I/2j_{\text{isat}}=1$, then the expression (32) can be linearized,

$$\phi_{\text{lin}} = \phi_0 + \ln \left[\cosh \left(\frac{\phi_{\text{rf}}}{2} \right) \right] + \delta\phi_{\text{lin}}, \quad (37)$$

$$\begin{aligned} \delta\phi_{\text{lin}}(r, t) = A \frac{\partial \nabla^2 \phi_{\text{rf}}(r, t)}{\partial t} = 4 \frac{L_{nc}^2}{r_0^2} \left(\frac{r^2}{r_0^2} - 1 \right) \frac{\phi_0}{2} \\ \times \text{sgn}[\cos(\omega t)] \sin(\omega t) \exp \left(-\frac{r^2}{r_0^2} \right). \end{aligned} \quad (38)$$

The time derivative of the absolute value of $\sin(\omega t)$ is equal to $\text{sgn}[\sin(\omega t)] \cdot \omega \cdot \cos(\omega t)$. As $\phi_{\text{rf}}(r)$ is a gaussian structure, the factor $-4/r_0^2$ appears on the LHS of Eq. (38). This equation can be simplified by considering the time evolution of the top of the structure for $r=0$.

$$\delta\phi_{\text{lin}}(0, t) = A \frac{\partial \nabla^2 \phi_{\text{rf}}(0, t)}{\partial t}, \quad (39)$$

$$= -4 \frac{L_{nc}^2}{r_0^2} \frac{\phi_0}{2} \text{sgn}[\cos(\omega t)] \sin(\omega t), \quad (40)$$

$$= \omega\tau_{\perp} \frac{\phi_0}{2} \text{sgn}[\cos(\omega t)] \sin(\omega t). \quad (41)$$

From Eqs. (40) and (41), it can be deduced that the relevant parameters defining the linearity domain for the rectification of the rf potential are

$$\frac{\Delta I(0, t)}{2j_{\text{isat}}} = -\frac{4L_{nc}^2}{r_0^2} \frac{\phi_{\text{rf}}(0, t)}{2} < -\frac{4L_{nc}^2}{r_0^2} \frac{\phi_0}{2} \ll 1 \quad (42)$$

or alternatively,

$$\frac{\Delta I(0, t)}{2j_{\text{isat}}} = \omega\tau_{\perp} \frac{\phi_{\text{rf}}(0, t)}{2} < \omega\tau_{\perp} \frac{\phi_0}{2} \ll 1. \quad (43)$$

$\omega\tau_{\perp}$ is strictly equivalent to $-4L_{nc}^2/r_0^2$. In that case, the time average potential of the Gaussian structure is $\langle \phi \rangle_t = \int_0^{2\pi} \phi_{\text{lin}} d\omega t = \phi_0/\pi - \ln(2)$ because the contribution of the time average linearized term $\delta\phi_{\text{lin}}$ is null. Temporally $\delta\phi_{\text{lin}}$ can be ignored compared to the potential amplitude at the top of the structure,

$$\phi(0, t) \approx \phi_0 + \ln[\cosh(\phi_{\text{rf}}(0, t)/2)]. \quad (44)$$

Spatially, the Gaussian potential structure is weakly modified. For $L_{nc}^2/r_0^2=1$, λ_{enl} , defined as the instantaneous enlargement of the structure, can be approached by integrating the Gaussian structure in space and dividing it with its amplitude. The time corresponding to $\omega t = \pi/2$ gives the maxi-

mum value for the correction $\delta\phi_{\text{lin}}$. This method allows us to obtain a space averaged enlargement along the amplitude of the potential structure to be compared to the characteristic length L_{nc} . This would enable us to check the dependence with r_0 , supposing that the Gaussian shape is conserved,

$$\begin{aligned} \lambda_{\text{enl}} = -\frac{\int [\phi_{\text{rf}}(r, \omega t = \pi/2)] dr}{\phi_0} \\ + \frac{\int \{[\phi_{\text{rf}}(r, \omega t = \pi/2)] + \delta\phi_{\text{lin}}\} dr}{\phi_0 + \delta\phi_{\text{lin}}(0, \omega t = \pi/2)}. \end{aligned} \quad (45)$$

Assuming that $\delta\phi_{\text{lin}} = \phi_0$, the expression can be simplified,

$$\lambda_{\text{enl}}[0, r_0] \approx \frac{\int_0^{r_0} \delta\phi_{\text{lin}} dr}{\phi_0}, \quad (46)$$

$$\lambda_{\text{enl}}[r_0, \infty] \approx \frac{\int_{r_0}^{\infty} \delta\phi_{\text{lin}} dr}{\phi_0}. \quad (47)$$

Both of these expressions of λ_{enl} come from the fact that the Laplacian of the Gaussian rf potential is negative while $|r| < r_0$ and is positive while $|r| > r_0$. $\lambda_{\text{enl}}[0, r_0]$ is the mean enlargement at the top part [Eq. (46)] of the Gaussian structure and $\lambda_{\text{enl}}[r_0, \infty]$ is the mean enlargement at the low part [Eq. (47)] of the Gaussian structure,

$$\frac{\lambda_{\text{enl}}[0, r_0]}{r_0} \approx -\frac{2L_{nc}^2}{r_0^2 \exp(1)}, \quad (48)$$

$$\frac{\lambda_{\text{enl}}[r_0, \infty]}{r_0} \approx \frac{2L_{nc}^2}{r_0^2 \exp(1)}. \quad (49)$$

Moreover, the sign of both these expressions depends on the time derivative of the Laplacian of the rf potential. According to Eq. (39), the sign of $\lambda_{\text{enl}}[0, r_0]/r_0$ does not change for $0 < \omega t < \pi/2$, and changes for $\pi/2 < \omega t < 0$. In the same way, the sign of $\lambda_{\text{enl}}[r_0, \infty]/r_0$ does not change for $0 < \omega t < \pi/2$, and changes for $\pi/2 < \omega t < 0$. Physically, this means that in the ascending phase the top part of the structure is spatially reduced and contracted [Eq. (48)], while the low part is increased and dilated [Eq. (49)]. On the contrary, in descending phase, the top part is increased and dilated [Eq. (49)] and the low part is reduced and contracted [Eq. (48)]. This is the most convenient way to approximate the evolution of this length during a period and to state that λ_{enl} is lower or approaching L_{nc}^2/r_0 . This value remains very small in the case of a linear theory (weak transverse current).

B. Nonlinear regime

If $\Delta I/2j_{\text{isat}} \gg 1$, the expression (32) becomes strongly nonlinear. The spatial behavior for the potential structure remains qualitatively similar to the linearized model. But due to the logarithm term, the reduction-contraction effect is minimized in ascending phase for the top part and in de-

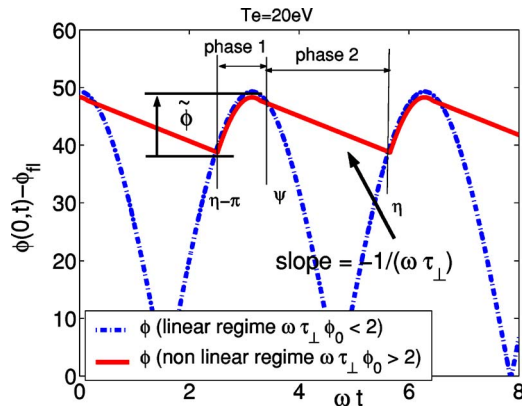


FIG. 3. (Color online) Schematic samples of linear and nonlinear rectified potential amplitude with transverse current as a function of time.

scending phase for the low part, while the increasing-dilatation effect is amplified in descending phase for the top part and in ascending phase for the low part.

In the course of time, we suppose that the summit of the potential structure remains a Gaussian of constant width even in the nonlinear case, $\Delta\phi(0,t) = -4\phi(0,t)/r_0^2$. This assumption will be examined below (see Sec. IV).

$$\phi(0,t) = \phi_{fl} + \ln[\cosh(\phi_{rf}/2)] - \delta\phi_{nolin}(0,t), \quad (50)$$

$$\delta\phi_{nolin}(0,t) = \ln\left(1 + \omega\tau_{\perp} \frac{\partial\phi(0,t)}{\partial\omega t}\right). \quad (51)$$

While $\phi < \phi_{fl} + \ln[\cosh(\phi_{rf}/2)]$ (phase 1, see Fig. 3), $\delta\phi_{nolin}$ is positive and weak compared to its linear expression,

$$\phi(0,t) \approx \phi_{fl} + \ln[\cosh(\phi_{rf}/2)]. \quad (52)$$

When ϕ passes over the solicitation (phase 2, see Fig. 3), the $\delta\phi_{nolin}$ becomes negative and strong enough to cause the summit of the structure to relax slowly when $\Delta I \rightarrow 2j_{isat}$. In that case, we can consider the extreme case for which the current saturates. Accordingly, the limit of the slope for $\phi(0,t)$ can be inferred from Eq. (30) (see Fig. 3),

$$\frac{\partial}{\partial\omega t} \phi(0,t) = -\frac{1}{\omega\tau_{\perp}}. \quad (53)$$

Expressions describing spatial behaviors would be extremely complex given the nonlinear enlargement of the structure. It can be stated, however, that while $\omega\tau_{\perp}\phi(r,t)$, all of the structure that fulfills the condition where $\Delta I \rightarrow 2j_{isat}$ is affected by a linear decreasing with a slope equal to $-1/(\omega\tau_{\perp})$. Consequently, the sole amplitude of the structure is diminished and the structure keeps a Gaussian shape. Whether the structure remains Gaussian in all kinds of regimes has to be assessed in order to achieve the analytical expression of ϕ .

C. Analytical expression for the rectified potential

From expression (3) under the assumptions of expression (51), we obtain the integral expression below,

$$\begin{aligned} & \int_0^{\omega t} \alpha [\exp(\phi_{rf}(0,t)/2) + \exp(-\phi_{rf}(0,t)/2)] d\omega t \\ &= \int_0^{\omega t} \left(1 + \omega\tau_{\perp} \frac{\partial\phi}{\partial\omega t}\right) \exp(\phi) d\omega t, \end{aligned} \quad (54)$$

$$\alpha = j_{esat}/2j_{isat}. \quad (55)$$

Bessel functions are then used to achieve the integration as follows:

$$\begin{aligned} & \int_0^{\omega t} \exp\left(\frac{\phi_0}{2} \cdot \cos(\omega t) + \frac{\omega t}{\omega\tau_{\perp}}\right) d\omega t = \int_0^{\omega t} \left[I_0\left(\frac{\phi_0}{2}\right) \right. \\ & \left. + 2 \sum_{k=1}^{\infty} I_k\left(\frac{\phi_0}{2}\right) \cos(k \cdot \omega t) \right] \exp\left(\frac{\omega t}{\omega\tau_{\perp}}\right) d\omega t. \end{aligned} \quad (56)$$

The analytic expression for $\phi(0,t)$ in a nonlinear case is finally obtained making the assumption that $\Delta\phi(0,t) = -4\phi(0,t)/r_0^2$ (Gaussian shape is conserved in the top part of the structure).

$$\phi(0,t) = \ln[\Phi_t(0,t) + \Phi_s + \tilde{\Phi}(0,t)], \quad (57)$$

$$\Phi_t(0,t) = \exp\left(-\frac{\omega t}{\omega\tau_{\perp}}\right) \left[1 - \alpha \left(\beta + 2 \sum_{k=1}^{\infty} \gamma_k\right)\right], \quad (58)$$

$$\Phi_s = \alpha\beta, \quad (59)$$

$$\tilde{\Phi}(0,t) = 2\alpha \sum_{k=1}^{\infty} \gamma_k [\cos(k\omega t) + k\omega\tau_{\perp} \sin(k\omega t)], \quad (60)$$

$$\beta = I_0\left(\frac{\phi_0}{2}\right) + I_0\left(\frac{-\phi_0}{2}\right), \quad (61)$$

$$\gamma_k = \frac{I_k\left(\frac{\phi_0}{2}\right) + I_k\left(\frac{-\phi_0}{2}\right)}{1 + (\omega\tau_{\perp})^2 k^2}. \quad (62)$$

In Eq. (57), $\phi(0,t)$ is the final analytical expression for the rectified potential (see Fig. 4). It is valid for linear and nonlinear behavior of potential structures and gives the amplitude of the maximum of this structure as a function of time. The general expression of $\phi(0,t)$ is composed of three terms.

The first one $\Phi_t(0,t)$ [Eq. (58)] describes the transient establishment of the rectified potential $\phi(0,t)$. It depends on $\omega\tau_{\perp}$ and $\phi_0/2$. When the time tends to infinity, this term becomes equal to 0.

Expression (57) can be simplified in the steady-state regime as follows:

$$\phi(0,t) = \ln(\Phi_s) + \ln\left[1 + \frac{\tilde{\Phi}(0,t)}{\Phi_s}\right]. \quad (63)$$

Then the first term of Eq. (63) represents the stationary component of the potential, which is slightly smaller than $\phi_0/2$. Supposing that $\Phi_t(0,t) = \Phi^e(0,t) = 0$, then $\phi(0,t) = \log \alpha + \log \beta = \phi_0/2 - \epsilon$, which is equal to the maximum time aver-

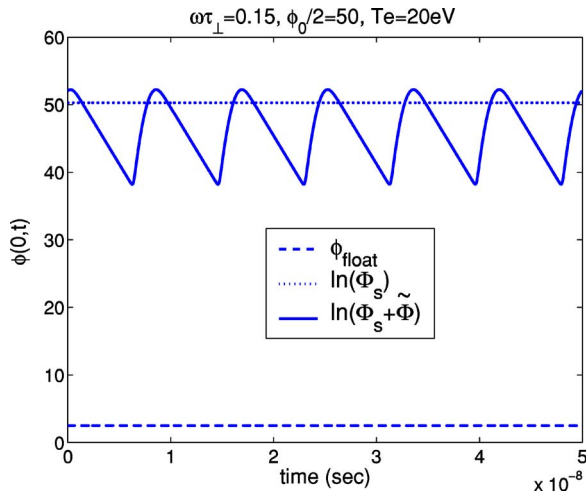


FIG. 4. (Color online) This figure gives the floating potential term, the stationary potential term, and the oscillatory term composing the analytical rectified potential in expression (57).

age potential that could be reached when the oscillatory term is close to 0. ϵ is a second-order correction and is small compared to ϕ_0 .

Now, the second term of Eq. (63) concerns the oscillatory part of the rectified potential with all harmonics. This term depends on $\phi_0/2$ and $\omega\tau_\perp$ and determines how the time average value increases. As a matter of fact, the time average value of the oscillatory part of the rectified potential is always negative because the transverse current has no dc component in accordance with Eq. (9).

When the time average of the oscillatory term is maximum, the time average potential $\langle\phi(0,t)\rangle_t$ is minimum and equal to $\phi_0/\pi - \ln 2$. While $\omega\tau_\perp \ll 1$, then the term in \cos is much higher than the term in \sin [see Eq. (64)]; the oscillatory signal is then unperturbed.

$$\frac{\tilde{\Phi}(0,t)}{\Phi_s} = \frac{2 \sum_{k=1}^{\infty} \gamma_k [\cos(k\omega t) + k\omega\tau_\perp \sin(k\omega t)]}{I_0\left(\frac{\phi_0}{2}\right) + I_0\left(-\frac{\phi_0}{2}\right)}. \quad (64)$$

On the contrary, if $\omega\tau_\perp > 1$, γ_k [Eq. (62)] becomes weak and the term in \sin is of the same order of magnitude as the term in \cos . The amplitude of the oscillatory term is close to zero and $\langle\phi(0,t)\rangle_t \rightarrow \phi_0/2$.

As $\phi_0\omega\tau_\perp$ increases, the time average potential $\langle\phi(0,t)\rangle_t$ increases from $\phi_0/\pi - \ln 2$ (linear behavior \approx no transverse currents) to $\phi_0/2 - \epsilon$ (nonlinear behavior \approx saturated transverse currents), which means that, for high value of ϕ_0 , $\langle\phi(0,t)\rangle_t/(\phi_0)$ is between $1/\pi$ and $1/2$ (see peaking criterion, Sec. VI B).

In the case where only one electrode is connected to the ground, the same expression would be obtained for ϕ , but with $\beta = 1 + I_0(\phi_0)$ and with $\gamma_k = I_k(\phi_0)/(1 + \omega^2\tau_\perp^2 k^2)$. For this configuration, the amplitude range of the time average potential $\langle\phi(0,t)\rangle_t$ is between $\phi_0/\pi - \ln 2$ and ϕ_0 .

In the first case, the plasma is driven by a rf electric field with symmetrical electrodes, and in the second case, the plasma is driven by the polarization of one electrode. This

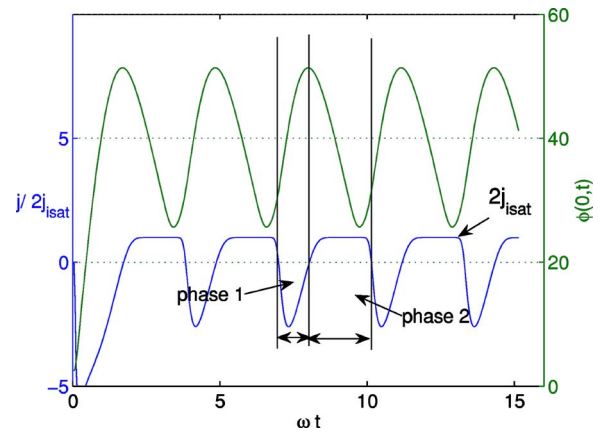


FIG. 5. (Color online) Comparison between transverse currents and the rectified potential at the summit of the oscillating Gaussian structure. Phases 1 and 2 are represented and their length depends on the parameter $\omega\tau_\perp$, which determines the slope of phase 2.

explains why our experiment yields results differing by a factor 2. However, it is important to know the position of the ground, i.e., the role played by the rf potential distribution on the rectified potential along a magnetic line. This problem could be developed in another work.

IV. NUMERIC SIMULATIONS OF rf RECTIFIED POTENTIAL IN A MAGNETIZED PLASMA AND COMPARISON OF RESULTS

The procedure consists of two sets of simulations. The purpose of the first set of simulations is to validate both our analytical model and the realistic behavior of the code. According to the analytical section, we use here a rf sinusoidal and Gaussian potential structure [Eq. (33)] located in the center of the grid perpendicular to the magnetic field (see Appendix A). This Cartesian mesh is composed of 256×256 cells. Boundary conditions are set to 0 V. Each cell length is shorter than L_{nc} and $dt\Omega_{ci} < 1$. The numerical method is based on the inversion of a sparse matrix using UMFPACK linear algebra routines.⁶ By varying the width of the potential structure and its amplitude, we obtain linear and nonlinear regimes that are tested by a 2D fluid code and the analytic theory developed in the previous section. Figure 5 demonstrates that the fluid code confirms the time shape of the current written in Sec. II A, i.e., the periodic current can be described according to Eq. (6) and its time average value is equal to 0. This figure also clearly illustrates that the current saturates during phase 2 as previously proposed in Fig. 3. These results partially validate the fluid code which was fully tested and verified in both linear and nonlinear cases.

The second set of simulations aims at comparing fluid and 2D particle-in-cell (PIC) calculations in a slab geometry. Here again, Gaussian shape was suitable to study the analytical expression of the rectified potential. A simple oscillating square shaped potential structure is applied in a plane perpendicular to the magnetic field for both PIC and fluid simulations. Analyses of such a simple shape allows us to easily measure the enlargement of the structure. The length of the flux tube varies so that we obtain linear and nonlinear re-

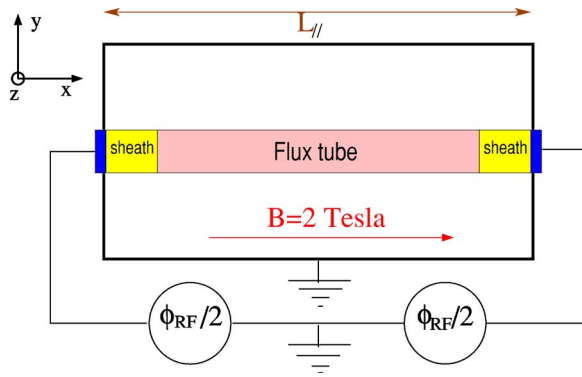


FIG. 6. (Color online) Scheme of the PIC simulation configuration. In that case the rf frequency is equal to 10 MHz and the boundary potential is 0 V.

gimes that are tested by 2D fluid code and the PIC code using the simulation parameters presented in Fig. 6. The PIC code used here is XOOPIC.²⁶ This code is an oriented-object electromagnetic particle-in-cell code written in C++. The boundaries are set to 0 V, $\Omega_{ce}dt < 1$, $\Omega_{pe}dt < 1$, and the parameters of the simulations are given in Table II.

Figures 7(a) and 7(b) depicts the potential structure in the flux tube ended by two electrodes polarized at $+1000 \sin(\omega t)$ V and $-1000 \sin(\omega t)$ V. The rectangular profile imposed by the square electrodes that are perfect conductors is slightly smoothed in strong potential gradient zones, but qualitatively, the width of the structure remains unchanged. This will be studied in Sec. IV B. In Fig. 7(b), the sheaths appear at the end of each flux tube. Each curve corresponds to four different times and allows us to observe the evolution of their length with respect to the potential amplitude of the electrodes. The maximum size of the sheaths

TABLE II. Typical plasma parameters corresponding to Figs. 9(a), 11(a), 9(b), and 11(b).

	Figs. 9(a) and 11(a)	Figs. 9(b) and 11(b)
n_i (m^{-3})	5×10^{17}	5×10^{16}
n_e (m^{-3})	5×10^{17}	5×10^{16}
T_i (eV)	20	"
T_e (eV)	20	"
$V_{rf}/2$ (V)	1000	"
ω (rad/s)	$2\pi \times 10^7$	"
Ω_{ci} (rad/s)	2×10^8	"
Ω_{pi} (rad/s)	9×10^8	3×10^8
m_i/m_e	1836	"
B (T)	2	"
λ_{De} (m)	5×10^{-5}	1.5×10^{-4}
L_P (mm)	5	50

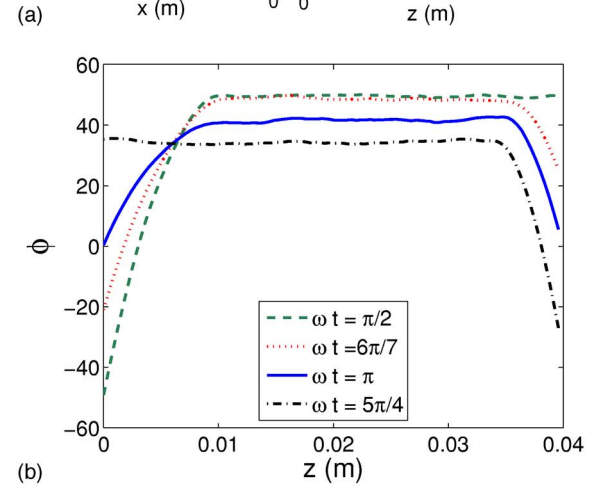
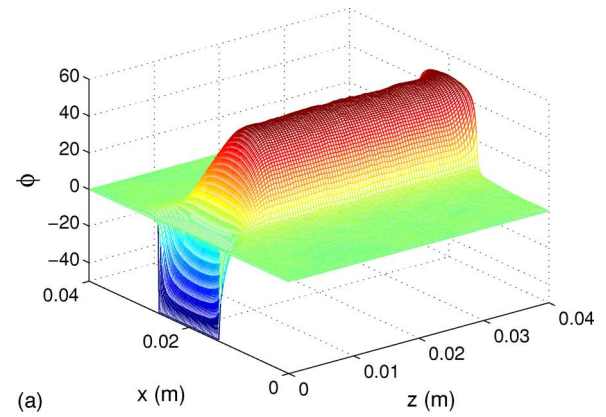


FIG. 7. (Color online) (a) Instantaneous rectified 2D potential map obtained from the PIC simulation in the configuration described in Fig. 6. (b) Instantaneous rectified 2D potential profiles along the magnetic field.

occurs when the rf potential is maximum at $V_{rf}/2 = 1000$ V or $\phi_{rf}/2 = 50$ and is approximately equal to 1 cm. Outside the sheaths, in quasineutral plasma, the potential is quasiconstant and depends on the presheath parameters. Nevertheless, the potential caused by the presheath is $0.7T_e/e = 14$ V according to Stangeby,²⁷ and this value is negligible compared to the potential observed in front of ICRH antennas, which is two to four orders of magnitude greater. The time evolution of the potential in the middle of the flux tube (that is always positive) will be studied in Sec. IV A.

A. Amplitude variation of the rectified potential structures: Temporal dynamic

This section aims at describing the temporal dynamic of a magnetized rf potential structure. The parameter $\omega\tau_\perp\phi_0/2$ defines the temporal potential dynamic as linear when it is lower than 1 and nonlinear when it is higher than 1. For each regime, fluid versus analytic results and fluid versus PIC results are compared for the plasma parameters in Table II.

For $\omega\tau_\perp\phi_0/2 < 1$, the linearized model given in expression (37) can be applied, and Fig. 8(a) shows that the temporal inertia of the potential structure is weak. Here the nonlinear analytical expression (57) is also valid. Transverse current effects are negligible and $\langle\phi\rangle_t \rightarrow \phi_0/\pi - \ln 2$.

The same results are obtained for a different set of simulations with $\omega\tau_\perp\phi_0/2 = 0.9$, while comparing fluid results

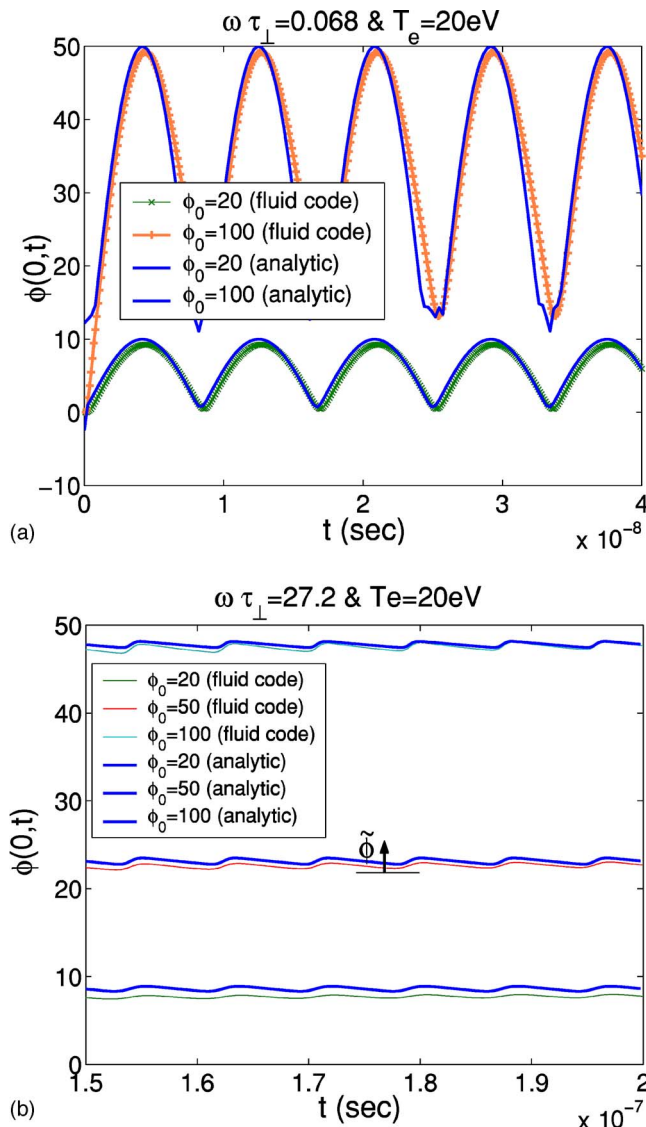


FIG. 8. (Color online) Amplitude of the Gaussian structure as a function of time for two values of $\omega \tau_{\perp} = -4L_{nc}^2/r_0^2$. (a) gives the potential rectification for two values of rf potential ($\phi_0/2=50, \phi_0/2=10$) with $1.7 \leq \omega \tau_{\perp} \phi_0/2 \leq 3.4$ (linear behavior). (b) shows the potential rectification for three values of rf potential ($\phi_0/2=50, \phi_0/2=25, \phi_0/2=10$) with $680 \leq \omega \tau_{\perp} \phi_0/2 \leq 1360$ (nonlinear behavior).

and PIC results. In that case, we do not use a Gaussian structure but simply a square shaped structure perpendicular to the magnetic field. It is equivalent to a square profile flux tube polarized with two square electrodes in front of each other. The distance between electrodes corresponds to the length of the magnetic line L_p (see Fig 6). Figure 9(a) shows a “linear” temporal dynamic of the top of the square shape structure for both fluid and PIC results that closely match. The magnetic line length is equal to 5 mm in the PIC simulation, which corresponds to a 2 mm magnetic line in the fluid simulation because the sheath lengths have to be subtracted. In that case, the sheath length is of the same order of magnitude as the magnetic line length and has to be taken into account in calculations. This linear dynamic is caused by the small length of the magnetic line which keeps the param-

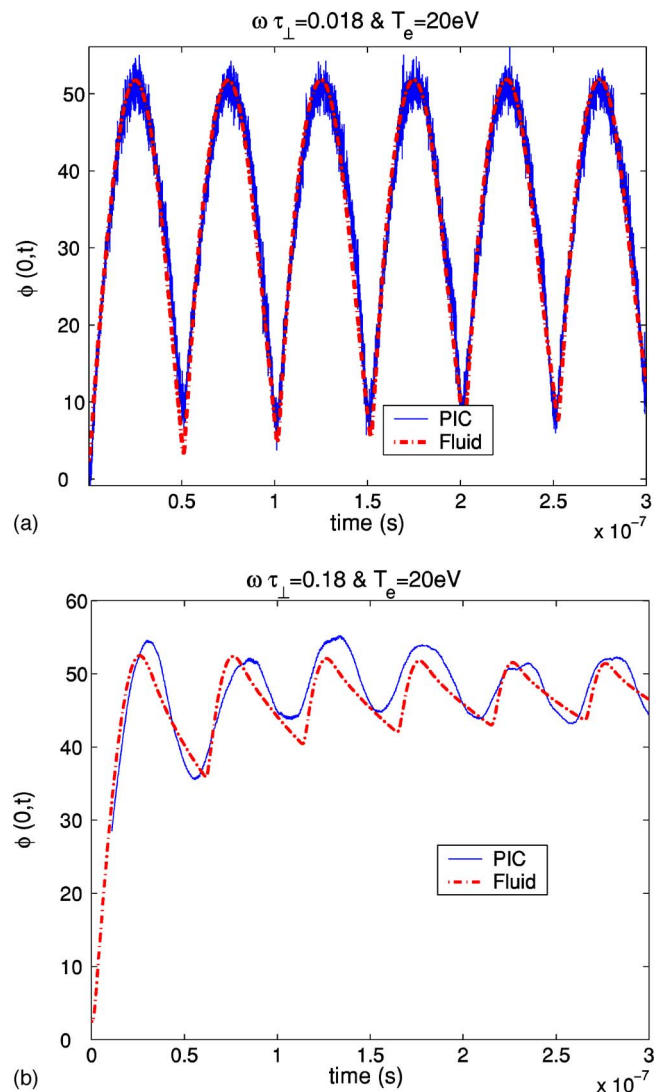


FIG. 9. (Color online) Amplitude of square shape structure vs time for two values of $\omega \tau_{\perp} = -4L_{nc}^2/r_0^2$. rf potential is normalized to $T_e = 20$ eV and its half amplitude is equal to 50. The rf square shaped potential is located in the middle of the simulation box and its width is 5 mm. For (a), $\omega \tau_{\perp} \phi_0/2 = 0.9$ (linear behavior), and for (b), $\omega \tau_{\perp} \phi_0/2 = 9$ (nonlinear behavior).

eter $\omega \tau_{\perp} \phi_0/2 < 1$. Here, transverse current effects are very weak, and the rectified potential follows the rf potential as predicted in the theory.

For $\omega \tau_{\perp} \phi_0/2 > 1$, Fig. 8(b) reveals that the code and the nonlinear analytic expression (57) are in good agreement for $\phi(0,t)$. Again, we demonstrate that on the one hand, $\max[\phi(0,t)] \approx \phi_0/2$, and on the other hand, $\phi^{\%} \rightarrow \pi/(\omega \tau_{\perp})$. The main effect of the rf sheath is indeed to rectify the potential signal. The transverse current makes the time average value increase up to $\phi_0/2$ when $\omega \tau_{\perp} \phi_0/2 \rightarrow \infty$. Again, fluid and PIC results are compared for the configuration described earlier [Fig. 9(a)] but with a magnetic line length 10 times greater. The parameter $\omega \tau_{\perp} \phi_0/2$ becomes then higher than 1 (here $\omega \tau_{\perp} \phi_0/2 = 9$), and the rectified potential in Fig. 9(b) follows a nonlinear dynamic with a strong inertia. The good agreement between “fluid rectified potential” and “PIC rectified potential” confirms the importance of the polarization current term kept in the simple fluid code. Here the magnetic

length is relatively long so that the sheath length can be ignored. The 2D3V PIC simulation reveals the inertia due to transverse current providing that all additional oscillations of the plasma [e.g., ion ($\Omega_{pi}=3\omega$) and electron ($\Omega_{pe}=125\omega$) acoustic waves] that may perturb the signal are filtered. The filtering step tends to smooth the asymmetry between the ascending and descending phase in PIC results. However, the amplitude and the characteristic frequencies given by the different codes are reasonably comparable.

B. Time average potential structures: Spatial behavior

At this stage of the study, the spatial behavior of the rectified potential structure has been analyzed with respect to the parameter L_{nc}^2/r_0^2 corresponding to the square ratio of the “characteristic enlargement” and the half-width of the potential structure. The spatial potential diffusion is negligible when L_{nc}^2/r_0^2 is lower than 1 and becomes significant when it is higher than 1. For each regime, fluid versus analytic results and fluid versus PIC results are compared for the plasma parameters listed in Table II.

Spatially, for $L_{nc}^2/r_0^2 > 1$, which means for a “diffusion length” greater than the width of the potential structure [Fig. 10(b)], the widening of the time average structure is obvious and averages L_{nc} , whereas the upper part increases as mentioned previously (see Sec. III B). The Gaussian shape seems to be conserved (see above). The amplitude and the width of the structure would have increased with the same ratio as determined by the saturated linear slope of phase 2.

For $L_{nc}^2/r_0^2 = 1$, the widening is less visible in Fig. 10(a) but the structure is modified in the same way.

The configuration of the PIC simulation is similar to those used for temporal dynamic (see Sec. IV A). Two examples of a rf square shape structure are given in Figs. 11(a) and 11(b). Results for fluid and PIC simulations are compared to investigate the enlargement of the potential structure. It is worth noting that the width of the time average structure remains unchanged for both PIC and fluid simulations. The peaking of the edges of the fluid structure in Fig. 10(a) results from the high value of $\nabla^2\phi$ (because of the square shape structure) or simply from the saturation of the transverse current at $2j_{\text{isat}}$. This means that the edge structure approaches a nonlinear regime whereas the center (for $r=0$) is strictly in a linear regime and its time average amplitude is approximately ϕ_0/π .

In the second simulation [Fig. 11(b)], $L_p=2$ cm, and hence $L_{nc}^2/r_0^2=0.026$. The potential profile of the dc square shape structure resulting from 2D fluid code seems to match the PIC potential structure. Figure 11(b) involves a nonlinear rectifying dynamic because $\omega\tau_{\perp}\phi_0/2 > 1$ and the amplitude of the time average potential structure is higher [$\langle\phi(r=0)\rangle_t \approx 45$] than the value obtained in a linear regime [$\langle\phi(r=0)\rangle_t \approx 35$ for low transverse current].

Nevertheless, PIC results are not always in accordance with fluid results. The latter can show a greater enlargement of the structure as well as a greater smoothing of the gradient variations in high potential gradient zones. This can be explained by the fact that the PIC code takes into account all

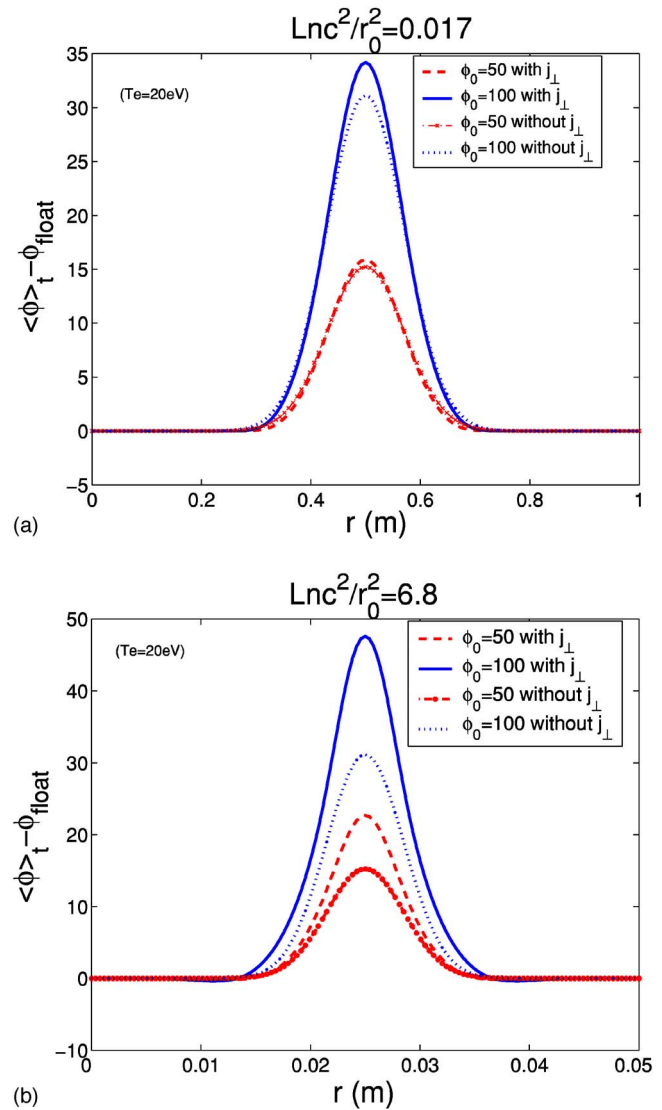


FIG. 10. (Color online) Spatial distribution of the time average rectified Gaussian structure for two values of rf potential normalized to $T_e=20$ eV ($\phi_0/2=50, \phi_0/2=100$) and for two values of $\omega\tau_{\perp}=-4L_{nc}^2/r_0^2$. For (a), $1.7 \leq \omega\tau_{\perp}\phi_0/2 \leq 3.4$ (linear behavior), and for (b), $680 \leq \omega\tau_{\perp}\phi_0/2 \leq 1360$ (nonlinear behavior).

current components, particularly the convective term, the plasma density variation, and ion and electron acoustic waves able to generate turbulent transport. All these phenomena can increase the potential diffusion perpendicular to the magnetic field.

V. EXTENSION OF THE DOMAIN FOR HIGH FREQUENCIES

The previous results have been obtained in the framework of low-frequency excitation $\omega=\Omega_{ci}$. However the criterion of linearity shown previously can be extended to frequencies higher than Ω_{ci} but lower than the ionic plasma frequency. An analytical equation of the polarization current can be obtained for all frequency ranges.

Equation (65) below results from the time derivative of Eq. (21) and is valid for all frequencies with $\Delta I/2j_{\text{isat}} = L_p \nabla_{\perp} \cdot j_{\perp}$ and $\mathbf{E}_{\perp} = -\nabla_{\perp} i T_e / e$. Moreover, the perturbation

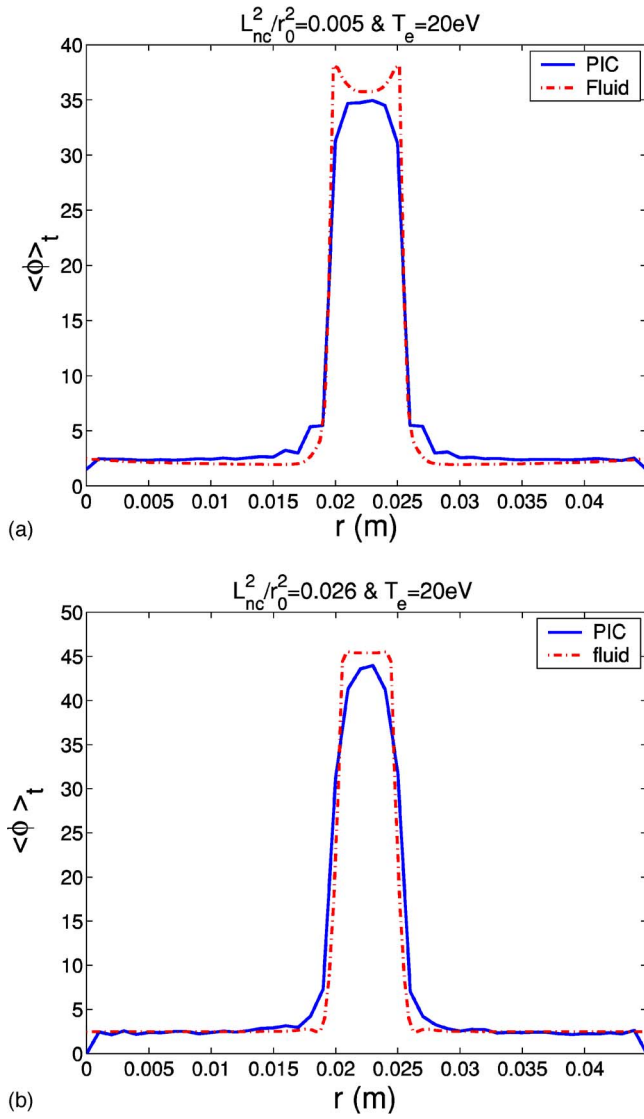


FIG. 11. (Color online) Spatial distribution of the time average rectified square shaped structure for two values of $\omega\tau_{\perp} = -4L_{nc}^2/r_0^2$. rf potential is normalized to $T_e = 20$ eV and half its amplitude is equal to 50. The rf square shaped potential is located in the middle of the simulation box. For (a), $\omega\tau_{\perp}\phi_0/2 = 1$ (linear behavior), and for (b), $\omega\tau_{\perp}\phi_0/2 = 5.2$ (nonlinear behavior).

induced by polarization currents is supposed weak, so that $\phi \approx \phi_{rf}^{rec}$ in a cylindrical geometry with $\phi_{rf}(r, t) = \phi_0(r)\cos(\omega t)$. The potential structure used is a Gaussian, $\phi_0(r) = \phi_0 \cdot \exp(-r^2/r_0^2)$ and $\phi_{rf}^{rec}(r, t) = \ln[\cosh(\phi_{rf}/2)]$. r_0 is the mean width of the potential structure.

$$\frac{1}{\Omega_{ci}^2} \frac{d^2}{dt^2} \left(\frac{\Delta I}{2j_{isat}} \right) + \frac{\Delta I}{2j_{isat}} = \frac{L_p \rho_{ci}}{2\Omega_{ci}} \frac{d\nabla^2 \phi_{rf}^{rec}(r, t)}{dt}. \quad (65)$$

The criterion of linearity can be expressed by $\Delta I/2j_{isat} < 1$. In that case, the potential term involving polarization currents ($\ln[\cosh(1 + \Delta I/2j_{isat})]$, see Eq. (31)) can be linearized while these currents stay smaller than 1.

At low frequency ($\omega < \Omega_{ci}$), Eq. (65) becomes

$$\frac{\Delta I}{2j_{isat}} = \frac{L_p \rho_{ci}}{2\Omega_{ci}} \frac{d\nabla^2 \phi_{rf}^{rec}(r, t)}{dt} < 1. \quad (66)$$

Supposing that time and space components of $\phi_{rf}^{rec}(r, t)$ are separable, ϕ , and $\phi \approx \phi_{fl} + \ln[\cosh(\phi_{rf}/2)]$ for a weak rectification, the expression of $\Delta I/2j_{isat}$ is given by Eq. (38) and then the final criterion of linearity at low frequency becomes as follows for $r=0$:

$$\frac{L_p \rho_{ci}}{r_0^2} \frac{\omega}{\Omega_{ci}} \phi_0 < 1. \quad (67)$$

At high frequency ($\omega \gg \Omega_{ci}$), the criterion of linearity results from

$$\frac{\Delta I}{2j_{isat}} = \Omega_{ci} \frac{L_p \rho_{ci}}{2} \nabla^2 \int [\phi_{rf}^{rec}(r, t) - \langle \phi_{rf}^{rec}(r) \rangle] dt < 1. \quad (68)$$

The only oscillating part of $\phi_{rf}^{rec}(r, t)$ has to be integrated. Consequently, the time average component $\langle \phi_{rf}^{rec}(r) \rangle$ is subtracted in expression (68) because it is filtered by the capacitive term appearing on the RHS of Eq. (65). The next step consists in integrating $\phi_{rf}^{rec}(r, t)$, which can be evaluated by using $[\phi_0(r)/2] \cos(\omega t) - \ln 2$ instead of $\ln(\cosh\{\phi_0(r)/2\} \cos(\omega t))$. When $\phi_0(r)/2$, $\ln 2$ can then be ignored. Finally, $|\cos(\omega t)|$ can be developed in Fourier series,

$$|\cos(\omega t)| = \frac{2}{\pi} \left(1 - 2 \sum_{n=1}^{\infty} \frac{(-1)^n}{4n^2 - 1} \cos(2n\omega t) \right). \quad (69)$$

The time integration of $\phi_{rf}^{rec}(r, t)$ gives

$$\begin{aligned} & \int [\phi_{rf}^{rec}(r, t) - \langle \phi_{rf}^{rec}(r) \rangle] dt \\ &= -\frac{\phi_0(r)}{2\omega} \frac{2}{\pi} \sum_{n=1}^{\infty} \frac{(-1)^n}{n(4n^2 - 1)} \sin(2n\omega t). \end{aligned} \quad (70)$$

And the maximum value of $\frac{2}{\pi} \sum_{n=1}^{\infty} (-1)^n / n(4n^2 - 1) \sin(2n\omega t)$ is close to $1/4.8$. Finally, the high-frequency criterion of linearity becomes as follows for $r=0$:

$$\frac{L_p \rho_{ci}}{r_0^2} \frac{\Omega_{ci}}{\omega} \phi_0 < 4.8 \quad (71)$$

with $\alpha = 1$.

For the same potential structure, the low-frequency criterion of linearity is inversely proportional to the high-frequency one. A qualitative symmetric behavior of the rectification is thus expected on each side of Ω_{ci} .

In the range of frequency verified by Eqs. (67) and (71), $\phi \approx \phi_0/\pi$. Out of the range of frequency verified by the same criteria of linearity [Eqs. (67) and (71)], the rectification of the rf potential can be obtained with the 2D PIC code. The simulated potential structure has a square shape as shown in Fig. 7(a). In simulations, the ratio ω/Ω_{ci} is changed by modifying the magnetic field and keeping ω and Ω_{pi} constant. The range of the ω/Ω_{ci} ratio covers all the ICRH scenarios from $2\Omega_{ci}$ to the fast wave electron heating (0.5 up to 5).²⁸ The parameters used in the 2D PIC simulations illustrated in Fig. 12 are the length of the flux tube $L_p = 4$ cm, the half-width of the structure $= 0.5$ cm, and $\phi_0 = 100$ at T_e

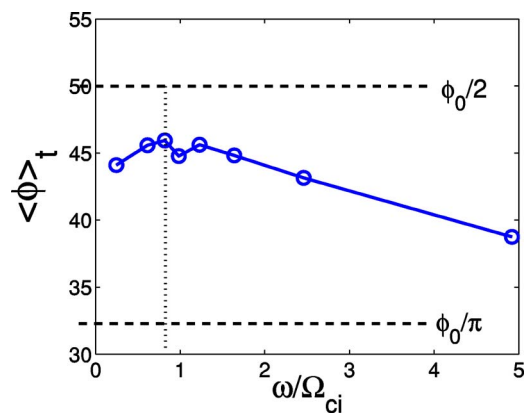


FIG. 12. (Color online) Time average amplitude of the rectified potential as a function of the ion cyclotron frequency normalized to a fixed rf frequency.

$=20$ eV. For a typical value of the magnetic field $B=2$ T, the criteria defined in Eqs. (67) and (71) give, respectively, $\omega/\Omega_{ci} < 0.05$ and $\omega/\Omega_{ci} > 4$. These limits are underestimated here because the square shape of the electrode imposes high transverse potential gradients which are located within a length smaller than the half-width of the structure. This explains why the time average values of $\langle \phi \rangle_t$ are never close to ϕ_0/π in Fig. 12.

The 2D PIC code results presented in Fig. 12 verified the qualitative symmetric behavior of the potential rectification around Ω_{ci} . They confirm that a strong rectification occurs near and around Ω_{ci} , however the small decrease at Ω_{ci} could be explained by a nonadiabatic response of the particles to the rf electric field.²⁹ The maximum dc potentials appearing around Ω_{ci} are equal to $0.46\phi_0$, which is close to the maximum theoretical value $0.5\phi_0$.

In a first approximation, our low-frequency fluid model can now be used to foresee the rectified dc potential map in front of the ICRH antenna for which the frequency is often greater than the typical cyclotron frequency in the edge plasma. The elaboration of a 2D fluid code valid for all frequencies is needed to obtain a more general quantitative approximation of $\langle \phi \rangle_t$ and should be explored in future works.

VI. APPLIED SAMPLE OF rf RECTIFICATION

This work finds concrete application in the response of the plasma to ICRH electric field excited in the vicinity of the ICRH antenna. Such antennas are used in Tokamaks to heat the plasma up to several million degrees Kelvin. They are recessed in the external wall of the toric chamber confining the plasma. One example appears in Fig. 13, which shows the lateral bumpers protecting the antenna from energetic plasma fluxes. This antenna is composed of two vertical straps radiating the waves and covered by a Faraday screen built with toroidal metallic strips set along two poloidal rows. In the same figure, the toroidal direction is horizontal, the poloidal one is vertical, and the radial direction is perpendicular to the plane of the figure.

The study of 2D potential structures in front of ICRH antennas was initially motivated by the apparition, on the antenna's structure, of hot spots^{5,20} in the upper left hand

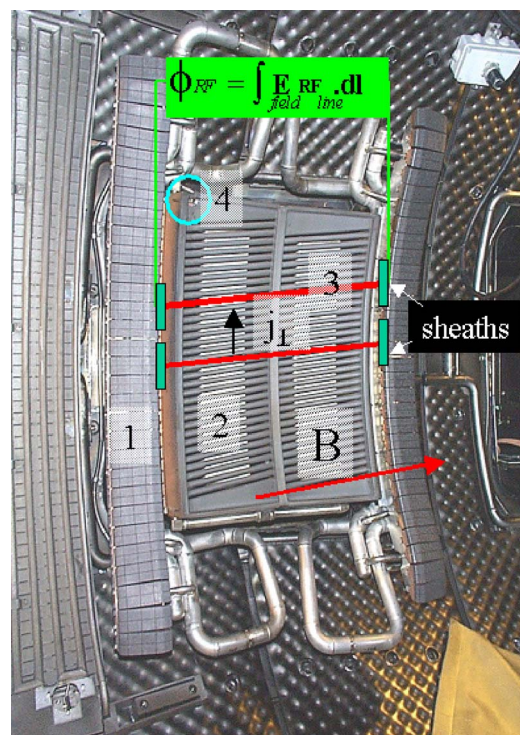


FIG. 13. (Color online) The labels (1) and (2) are, respectively, the bumpers protecting the antenna and the straps radiating the waves. Magnetic lines (3) and sheaths are represented in front of the antenna. The hot spot appears (4) on the upper left hand corner of the Faraday screen.

corner or in the lower right hand corner with respect to magnetic field direction (see Fig. 13). The main component of rf electric field radiated by the antenna straps is along y (poloidal direction). But the mismatch orientation (and other effects) between the Faraday screen and the magnetic field lines creates a parallel electric field by projection of the poloidal component.^{19,30} The integration of this parallel electric field along the magnetic lines between the bumpers (see Fig. 13) gives a non-null rf electrostatic potential³¹ able to induce rf sheaths. Magnetic lines can be seen as flux tubes ended by rf sheaths which rectify the rf potential and are able to create high dc potential structures in front of the Faraday screen of the antenna. These structures are able to accelerate parallel ion fluxes and convective fluxes onto the antenna's surface and dangerously heat the materials to finally create hot spots.

A. Correlation between antenna potential map and hot spot formation

The rf potential map deduced from the ICANT code³² computations reveals the high peaking potential areas at the top and at the bottom of the antenna structure (see Fig. 15). The ICANT code is a wave code computing the electric fields that occur near the surface of the antenna structure (see Fig. 14). The successive poloidal potential peaks and potential holes correspond to the successive strips of the Faraday screen. The ICANT electric field map was performed with a plasma density of $5 \times 10^{18} \text{ m}^{-3}$, a magnetic field $B_0=3$ T, a magnetic line angle of 7° , a frequency of 48 MHz, and a radial distance of 4 cm from the Faraday screen.

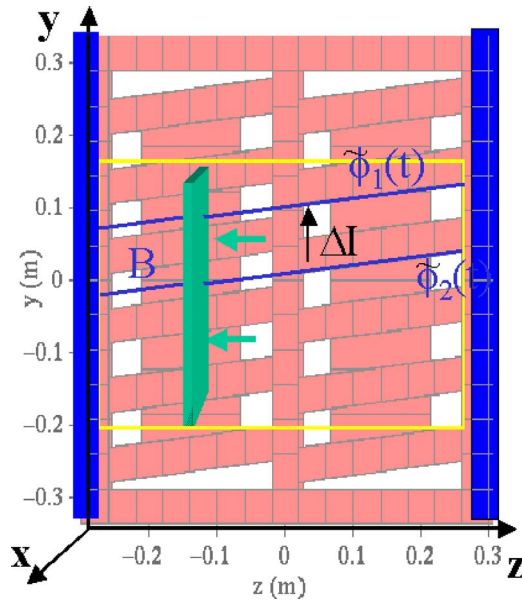


FIG. 14. (Color online) Schematic antenna structure used in the ICANT code to compute the electric fields in the vicinity of the ICRH antenna. The plane perpendicular to the two magnetic lines is the simulation plane.

The rf potential map ϕ_{rf} is obtained by integrating E_p along B_0 between both bumpers. Due to the small angle of the magnetic field compared to the straight antenna structure, only half of the line crosses in front of the antenna whereas the other half is out of the radiating area. This is the reason why E_p in the first part is not offset by E_p in the second part, even for a $0-\pi$ phasing of the straps. The integration of E_p results in a significantly high ϕ_{rf} at both the bottom and top part of the antenna structure. In these areas, rf potentials are largely rectified due to the nonlinear response of the rf sheath, and dc structures are of the order of half the initial amplitude of ϕ_{rf} in the range from 0.5 up to 2 kV. The high dc potential peaks accelerate ion fluxes in the sheaths and create strong convective fluxes around these dc potential structures, which tend to deviate plasma fluxes onto either the upper or the lower part of the structure of the antenna depending on the magnetic field direction. Moreover, the distribution of the deposition flux on the antenna structure is confined near its corner. Different reasons can be invoked, such as magnetic lines angle, parallel currents in the antenna structure, and nonhomogeneous plasma.⁵ From these results, the simulation possibilities can be used to obtain a peaking criterion to be compared to the one given by expression (57).

B. Peaking criterion

The parametric study consists in testing how the time average potential amplitude is rectified with respect to the two parameters ϕ_0 and $\omega\tau_\perp$, which are, respectively, the initial rf potential amplitude and the relaxing normalized time of the potential structure. The model is run for an array of ϕ_0 (normalized to $T_e=20$ eV) and $\omega\tau_\perp$ values ranging from 1 to 100 and from 0.01 to 10, respectively. Doing so, we obtain each isocurve corresponding to each peaking ratio equal to

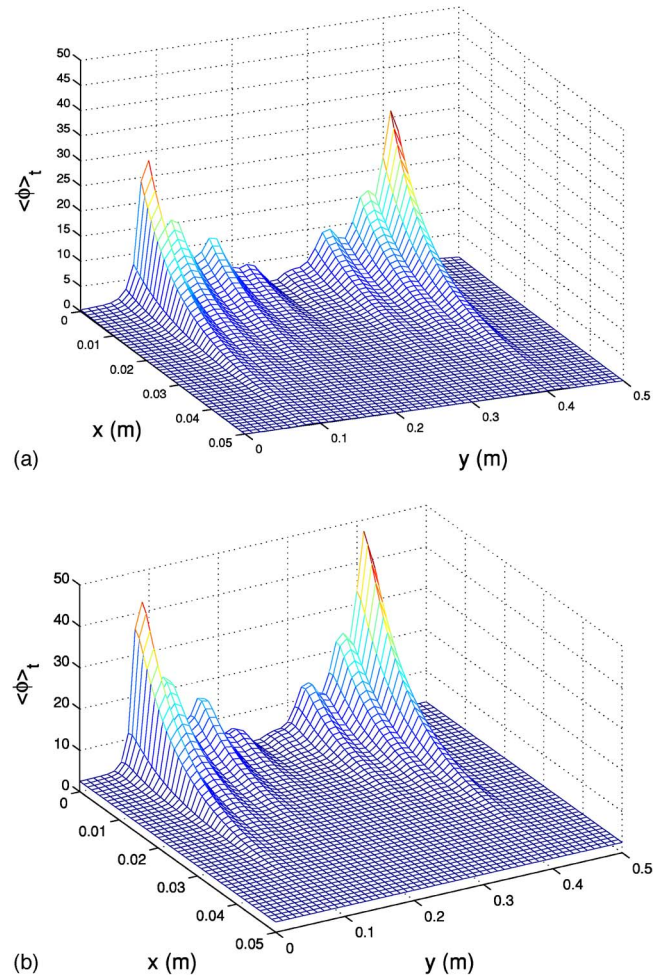


FIG. 15. (Color online) (a) is the dc rectified potential map computed thanks to ICANT code results in a poloidal plane in front of the ICRH antenna without transverse current effects. (b) is the dc rectified potential map with transverse current effects. The potential decreases exponentially when the radial coordinate increases because the wave is evanescent. The poloidal direction is along “y.”

$\langle \phi(r=0) \rangle_t / \phi_0(r=0)$, i.e., the time average amplitude of the rectified potential with currents over the maximum amplitude of the rf potential.

The first conclusion about this criterion is the good agreement between code and analytical results expected for $\langle \phi(0,t) \rangle_t / \phi_0 = 0.45$. This is due to the quality of the interpolation obtained with a finite number of simulations. Secondly, the structures are not smoothed in the sense of a pure diffusion. On the contrary, they are peaked in the upper part, and dilated in the lower part. All these observations are made by using the time average value of the amplitude distribution during one period. Thirdly, typical Tore Supra potential structures are centimetric wide ($0.2 < \omega\tau_\perp < 4$) and their amplitudes range from 100 to 1000 V ($5 < \phi_0 < 50$). These parameters are provided by the potential map computed by the ICANT code³² (see Fig. 15), and are mainly concerned with our nonlinear theory. This map would help to assess the amplitude of potential structures able to create high localized convective fluxes. To define the ITER zone in Fig. 16, we have assumed that edge plasma parameters and electric properties of the antennas in ITER and Tore Supra are the same.

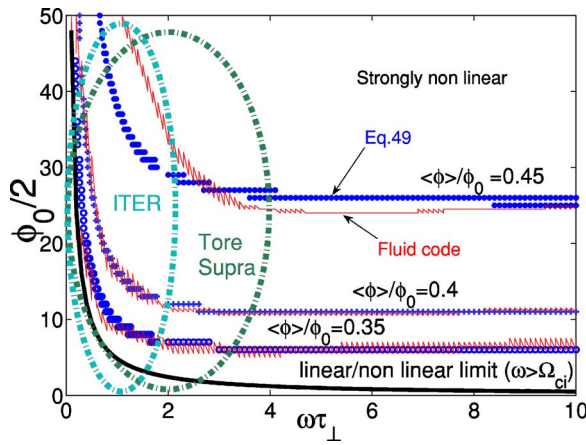


FIG. 16. (Color online) Typical domain for ICRH Tore Supra's antenna and a typical ICRH ITER's antenna compared to isocurves corresponding to the ratio $\langle\phi\rangle/\phi_0$ as a function of $\omega\tau_{\perp} = -4L_{nc}^2/r_0^2$ for a Gaussian structure at $T_e = 20\text{ eV}$.

Under these conditions, the discrepancies between ITER and Tore Supra zones result from the geometry of the Faraday shield and the length of the open magnetic field line in front of the antenna. As the ITER antenna structure is about two times bigger than the Tore Supra one, all geometrical parameters are multiplied by a factor of 2. Anyway, the ITER case should have a nonlinear rectification of the rf potential and the dc potential peak due to rf rectification will be conserved as well as the possibility of forming hot spots. Thus, the near electric field in front of antenna should be optimized to reduce as much as possible the rf potential.³³

VII. CONCLUSION

The elaboration of a simple flux tube model able to exchange transverse polarization currents in magnetized plasmas allows us to obtain an analytical expression for the rectified potential of open magnetic field lines. From this model we deduced the linearized expression of ϕ , which gives the same time average potential with and without current because $\omega\tau_{\perp}\phi_0 \ll 1$: $\langle\phi\rangle_t = \phi_0/\pi - \ln 2$ for ϕ_{rf} and ϕ_{fl} . Spatial widening of the structure is described and expressed as a function of the length L_{nc} depending on the polarization current. From the nonlinear expression of ϕ , assuming that the top of the structure remains Gaussian with an unperturbed width, we assessed the relaxation time τ_{\perp} , similar to the one used for a capacitive charge. In the nonlinear case $\omega\tau_{\perp}\phi_0$, and then $\langle\phi\rangle_t \rightarrow \phi_0/2$. No tractable expression for the spatial widening of the potential has been obtained, however. The main physical effect of transverse polarization currents on the potential structures is to intensify the inertia of the rectified potential dynamic and to smooth small-scale structures ($<L_{nc}$). As the parameter $\omega\tau_{\perp}\phi_0$ augments, the oscillating rectified potential structure becomes increasingly “frozen” in the plasma near its half maximum amplitude. These results are in good agreement with the first set of simulations and our 2D fluid code confirms that the assumption $\nabla^2\phi(0,t) = (-4/r_0^2)\phi(0,t)$ is valid. The second set of simulations involving the fluid code versus PIC code demonstrates the validity of the 2D fluid code, which ignores all other transport

phenomena and plasma waves. Transverse polarization currents are the major effect acting in the potential structure dynamic. By means of the 2D PIC code XOOPIC, the behavior of the potential rectification can be extended to a frequency range covering all the scenarios of the heating and current drive used in fusion devices. For $\omega > \Omega_{ci}$, the rectification is nonlinear out of the linearity criterion domain established analytically for weak polarization currents as for $\omega < \Omega_{ci}$. This high-frequency limit for the criterion of linearity is approximately equal to $4\Omega_{ci}$ for a Gaussian centimetric structure with $\phi_0 = 100$ at $T_e = 20\text{ eV}$, whereas the low frequency limit is equal to $\Omega_{ci}/20$.

The potential peak criterion for frequencies greater than ion cyclotron frequency is then applied to the map of the rectified potential obtained in the Tore Supra case. The conclusion is that the behavior of this rectified potential in front of the ICRH antenna can be considered as nonlinear.

Under these conditions, the dc potentials can increase values up to half the amplitude of the rf potential or up to 1.5 the value of the dc rectified potential without current. dc potentials with polarization currents are thus up to 50% higher than those obtained without the polarization current effects. Previous works conducted in this field underestimated the value of the rectified potential. We propose that overall, preceding evaluations of the power flux deposited on the wall should be revised. As a matter of fact, a high dc potential peak can accelerate ions in the sheaths and create convective fluxes in the corner of the antenna's structure, which can generate hot spots on the wall.

All the aforementioned results have been obtained for comparable OMFL lengths. In the near future, it would be useful to carry out studies focused on interactions between different OMFL lengths. These studies involve more complex configurations found in corners of antennas, and at the boundary of bumpers or limiters. This could extend the study of polarization currents in the whole SOL to monitor the effect of polarized magnetic lines connected to ICRH antennas. In addition, such a model could be applied in magnetized plasma rf discharges and rf magnetrons providing that the current induced by collisions remains small compared to the polarization current.

APPENDIX A: FLUID CODE

This code is based on Eq. (32) expressed in the form of Eq. (A1),

$$1 - \exp(\phi_{fl} + \ln\{\cosh[\phi_{rf}(x,y,t)]\} - \phi_{x,y,t}) = A \frac{\partial \nabla^2 \phi(x,y,t)}{\partial t}. \quad (\text{A1})$$

This equation is approximated by a finite-difference scheme implicitly in space and explicitly in time. One obtains the discrete equation

$$\begin{aligned}
& 1 - \exp(\phi_{\text{fl}} + \ln\{\cosh[\phi_0(x_i, y_j)\sin(\omega t)]\} - \phi_{i,j,t}) \\
& + \frac{A}{\Delta t} \left[\frac{\phi_{i+1,j,t} - 2\phi_{i,j,t} + \phi_{i-1,j,t}}{(\Delta x)^2} \right. \\
& \left. + \frac{\phi_{i,j,t+1} - 2\phi_{i,j,t} + \phi_{i,j,t-1}}{(\Delta y)^2} \right] \\
& = \frac{A}{\Delta t} \left[\frac{\phi_{i+1,j,t+1} - 2\phi_{i,j,t+1} + \phi_{i-1,j,t+1}}{(\Delta x)^2} \right. \\
& \left. + \frac{\phi_{i,j,t+1+1} - 2\phi_{i,j,t+1} + \phi_{i,j,t-1+1}}{(\Delta y)^2} \right]. \quad (\text{A2})
\end{aligned}$$

This equation gives the list of coefficients to define each line of the sparse multidagonal matrix corresponding to each linear equation of the system to be solved. With $m=\max(i)$ and $n=\max(j)$, we can apply $m \cdot n$ times this equation, and we deduce a system of $m \cdot n$ equations with $m \cdot n$ unknowns corresponding to each value of $\phi_{i,j}$ at the time t in the 2D space perpendicular to the magnetic field. All the boundaries are set to 0 V so that $\phi_{0,j,t} = \phi_{i,0,t} = \phi_{m,j,t} = \phi_{i,n,t} = 0$. The topology of $\phi_{\text{rf}}(x_i, y_j, t)$ is defined as a Gaussian,

$$\phi_{\text{rf}}(x_i, y_j, t) = \phi_0 \exp\left(-\frac{x_i^2 + y_j^2}{r_0^2}\right) \sin(\omega t). \quad (\text{A3})$$

r_0 is the width of the Gaussian for an amplitude equal to $\phi_0/\exp(1)$. The linear system is presented under matrix form in Eq. (A4),

$$M \cdot \phi = \mathbf{f}(\phi_{\text{rf}}). \quad (\text{A4})$$

$\mathbf{f}(\phi_{\text{rf}})$ is a vector with the length $m \cdot n$ equivalent to the LHS term of the discrete Eq. (A2). M is the square, sparse, and symmetric pentadiagonal matrix with the dimension $(m \cdot n)^2$ gathering all coefficients involved in front of each $\phi_{i,j}$ in the RHS term of Eq. (A2). From here, the matrix M has to be inverted to solve all $\phi_{i,j}$,

$$\phi = M^{-1} \mathbf{f}(\phi_{\text{rf}}). \quad (\text{A5})$$

The method used to invert the matrix takes part of the linear mathematics libraries called UMFPACK³⁴, which is able to achieve these operations with a minimum of memory and time. Schematically, this method is similar to a classical LU factorization with $M=L \cdot U$, but here M is factorized in four matrices so that $M=L \cdot U \cdot P \cdot Q$. Then, it becomes easy to solve the example in Eq. (A6) by applying Eq. (A7),

$$M \cdot \mathbf{x} = \mathbf{b}, \quad (\text{A6})$$

$$\mathbf{x} = Q \cdot \{U[L(P \cdot \mathbf{b})]\}. \quad (\text{A7})$$

This operation has to be repeated at each time step to solve the problem in time.

- ¹A. Metze, D. W. Ernie, and H. J. Oskam, J. Appl. Phys. **60**, 3081 (1986).
- ²K. U. Riemann, J. Appl. Phys. **65**, 999 (1989).
- ³A. M. Pointu, Appl. Phys. Lett. **48**, 762 (1986).
- ⁴V. A. Godiak and N. Sternberg, Phys. Rev. A **42**, 2299 (1990).
- ⁵L. Colas, L. Costanzo, C. Desgranges, S. Brémond, J. Bucalossi, G. Agari, and V. Basiuk, Nucl. Fusion **43**, 1 (2002).
- ⁶E. Faudot, S. Heuraux, and L. Colas, Czech. J. Phys. **53**, 911 (2003).
- ⁷V. A. Godyak and A. A. Kuzovnikov, Fiz. Plazmy **1**, 496 (1975).
- ⁸J.-J. Gonzalez and A. Shabalin, Plasma Sources Sci. Technol. **12**, 317 (2003).
- ⁹K.-U. Riemann and T. Daube, J. Appl. Phys. **86**, 1202 (1999).
- ¹⁰V. Rozhansky, A. A. Ushakov, and S. P. Voskoboynikov, Nucl. Fusion **39**, 613 (1999).
- ¹¹K. Gunther and A. Carlson, Contrib. Plasma Phys. **34**, 484 (1994).
- ¹²M. Ashraf and M. G. Rusbridge, Plasma Phys. Controlled Fusion **29**, 969 (1987).
- ¹³A. V. Nedospasov and D. A. Uzdensky, Contrib. Plasma Phys. **34**, 478 (1994).
- ¹⁴A. Carlson, Phys. Plasmas **8**, 4732 (2001).
- ¹⁵V. Rozhansky, S. P. Voskoboynikov, E. G. Kaveeva, D. P. Coster, and R. Schneider, Nucl. Fusion **41**, 613 (2001).
- ¹⁶P. Verplancke, Contrib. Plasma Phys. **34**, 484 (1994).
- ¹⁷D. A. D'Ippolito, J. R. Myra, J. Jacquinet, and M. Bures, Phys. Fluids B **10**, 3603 (1993).
- ¹⁸D. A. D'Ippolito and J. R. Myra, Phys. Plasmas **7**, 3301 (2000).
- ¹⁹D. A. D'Ippolito, J. R. Myra, P. M. Ryan, E. Righi, J. Heikkinen, P. U. Lamalle, and J.-M. Noterdaeme, Nucl. Fusion **42**, 1357 (2002).
- ²⁰M. Becoulet, L. Colas, S. Pecoul, J. Gunn, P. Gendrih, A. Becoulet, and S. Heuraux, Phys. Plasmas **9**, 2619 (2002).
- ²¹F. L. Waelbroeck, Phys. Rev. E **65**, 066407 (2002).
- ²²M. Brambilla, *Kinetic Theory of the Plasma Waves*, Oxford Science Publications (Clarendon Press, 1998).
- ²³D. Zhong-Ling, Y.-N. Wang, and T.-C. Ma, Phys. Rev. E **65**, 036403 (2002).
- ²⁴M. A. Sobolewski, Phys. Rev. E **62**, 8540 (2000).
- ²⁵S. I. Braginskii, Rev. Plasma Phys. **1**, 215 (1965).
- ²⁶J. P. Verboncoeur, A. B. Langdon, and N. T. Gladd, Comput. Phys. Commun. **87**, 199 (1995).
- ²⁷P. C. Stangeby, *The Plasma Boundary of Magnetic Fusion Devices* (IOP, Bristol, 2000).
- ²⁸A. Becoulet, Plasma Phys. Controlled Fusion **38**, A1 (1996).
- ²⁹B. M. Lamb, G. Dimonte, and G. J. Morales, Phys. Fluids **27**, 1401 (1984).
- ³⁰F. Perkins, Nucl. Fusion **29**, 583 (1989).
- ³¹J.-M. Noterdaeme and G. V. Oost, Plasma Phys. Controlled Fusion **35**, 1481 (1993).
- ³²S. Pecoul, S. Heuraux, R. Koch, and G. Leclert, Comput. Phys. Commun. **146**, 166 (2002).
- ³³L. Colas, S. Heuraux, S. Brémond, and G. Bosia, Nucl. Fusion **45**, 767 (2005).
- ³⁴T. A. Davis, *UMFPACK Version 4.0 User Guide* (<http://www.cise.ufl.edu/research/sparse/umfpack/v4.0>) (Department of Computer and Information Science and Engineering, University of Florida, Gainesville, FL, 2002).